The ligand-mediated affinity of escort proteins determines the directionality of lipophilic cargo transport

Yi-Yun Cheng[1,2], **Yun-Fang Huang**[1], **Hsin-Hui Lin**[1], **Wun-Shaing Wayne Chang**[2*], **Ping-Chiang Lyu**[1,3*]

***For correspondence:**
lslpc@life.nthu.edu.tw (PCL);
wayne@nhri.org.tw (WSWC)

[1]Institute of Bioinformatics and Structural Biology, National Tsing Hua University, Hsinchu, Taiwan; [2]National Institute of Cancer Research, National Health Research Institutes, Zhunan, Taiwan; [3]Department of Medical Sciences, National Tsing Hua University, Hsinchu, Taiwan

Abstract Intracellular cargo transport is a highly dynamic process. In eukaryotic cells, the uptake and release of lipophilic ligands are executed by escort proteins. However, how these carriers control the directionality of cargo trafficking remains unclear. Here, we have elucidated the unliganded structure of an archetypal fatty acid-binding protein (FABP) and found that it possesses stronger binding affinity than its liganded counterpart towards empty nanodiscs. Titrating unliganded FABP and nanodiscs with long-chain fatty acids (LCFAs) rescued the broadening of FABP cross-peak intensities in HSQC spectra due to decreased protein-membrane interaction. Crystallographic studies revealed that the tails of bound LCFAs obstructed the charged interfaces of the FABP–nanodisc complexes. We conclude that the lipophilic ligands, by taking advantage of escort proteins with high conformational homogeneity and nanodiscs as the third interaction partner involved in this transport study, participate directly in the control of their own transportation in an irreversible, unidirectional fashion.

Introduction

Intracellular cargo transport is the cornerstone of many biological processes, including cellular metabolism, energy homeostasis, neuron development and organelle function. In eukaryotic cells, a number of escort proteins have evolved to shuttle lipophilic cargos from external or internal environments to distinct subcellular compartments (***Herrmann et al., 1999; Furuhashi and Hotamisligil, 2008; Slater et al., 2016***). Among these escort proteins, the cytosolic fatty acid-binding proteins (FABPs) are the archetypal lipid chaperones for long-chain fatty acids (LCFAs) and certain other energy-rich lipophilic ligands (***Flower, 1996; Hertzel and Bernlohr, 2000; Smathers and Petersen, 2011; Hotamisligil and Bernlohr, 2015***). The FABP carriage system is essential because 1) it minimizes the potential toxicity of free non-esterified LCFAs; 2) it facilitates the rapid cellular uptake and regulatable transport of LCFAs in concert with metabolic demands; and 3) it permits LCFAs to traverse intracellular space to various sites of utilization, e.g. to the endoplasmic reticulum for transacylation and to the nucleus for transcriptional regulation (***Glatz and van der Vusse, 1996; Boden, 2008***). Upon binding to LCFAs, FABPs themselves may enter the nucleus to activate several transcription factors such as PPARs (peroxisome proliferator-activated receptors) and ERRs

(oestrogen-related receptors) for downstream cellular signalling, metabolic reactions and immune responses (***Tan et al., 2002; Michalik et al., 2004; Noy, 2007***).

Considerable evidence suggests that once absorbed by cell membrane phospholipids, LCFAs are sequestered and delivered by FABPs (***Stremmel et al., 2001; Bazinet and Layé, 2014***) in a manner probably similar to the substrate-binding proteins (***Marinelli et al., 2011***). Despite substantial efforts to determine the key structural factors contributing to lipophilic cargo binding (***Lücke et al., 1996; Hodsdon and Cistola, 1997; Xiao et al., 2016***), the precise mode of how LCFAs are directionally transported by FABPs from a specific donor membrane to a target acceptor membrane or protein remain largely in dispute (***Furuhashi and Hotamisligil, 2008***). One major reason for this ambiguity is inadequate research on the role of the phospholipid membrane in cargo trafficking, in that the uptake and release of lipophilic ligands depend not only on the ligand competition between escort proteins and ligand donors/acceptors but also on the selective affinities of unliganded and liganded escort proteins towards ligand donors/acceptors. Recent NMR and protein engineering studies revealed that the helical portal motif of FABPs for ligand entry was capable of reversibly transferring LCFAs across the plasma and intracellular membranes (***Kim and Storch, 1992; Corsico et al., 1998; Thumser and Storch, 2000; Weisiger, 2002***). However, owing to the uncertain conformational homogeneity (***He et al., 2007; Guariento et al., 2009***) and the lack of appropriate biomembrane mimetics in past research (***Ceccon et al., 2013; Silvaroli et al., 2016***), it is still unclear whether lipophilic ligands can be reversibly transported and how escort proteins control the directionality of cargo trafficking.

In this article, we utilized *Drosophila* FABP as a model system to assess the hypothesis of a directionality-controlled mechanism in escort proteins. An improved purification strategy was provided to separate the liganded-like and unliganded forms of FABP. The latter exhibited very high conformational homogeneity, allowing us to verify how different forms of FABP interact differently with lipid bilayer membranes. By employing membrane mimetic nanodiscs for NMR experiments, we were able to increase the tumbling rates of FABP–nanodisc complexes to reveal the residue-based membrane-interacting region of escort protein. Our structural analyses demonstrated that unliganded FABP has a much stronger binding affinity than its liganded counterpart to empty nanodiscs. Crystallographic studies showed that the LCFAs participate in their own transportation by disturbing the charged interfaces between FABPs and lipid membranes with aliphatic tails. Together, these results clearly suggest that the membrane-binding capacity of escort proteins is regulated by their target ligands, ultimately facilitating irreversible unidirectional lipophilic cargo transfer.

Results

Escort proteins with high conformational homogeneity are important for determining the regulatory mechanism of membrane-associated cargo transport

The escort protein represented herein is a *Drosophila* brain-type FABP (dFABP) that exists mainly in glial cells and localizes in both the cytoplasm and the nucleus (***Anthony et al., 2005; Gerstner et al., 2011a***). Its movement from the cytoplasm to the nucleus in response to diurnal regulation and memory consolidation raises the question of how ligands trigger dFABP function. Although earlier biochemical assays of FABPs tolerated the minor heterogeneity in assessing the nature of their ligand binding (***Tochtrop et al., 2002; Velkov et al., 2005***), we believed that studying escort proteins with high conformational homogeneity would illustrate the apparently dynamic lipid transport process. To clarify whether insufficient conformational homogeneity may impede further research on the interaction between FABPs and membrane mimetics, we compared the two apo forms of dFABP isolated by the existing method (denoted as the urea-treated method) and by the newly improved two-stage purification procedure with the use of the reagent GuHCl to induce partial unfolding (denoted as the GuHCl-purification method, see ***Supp. Fig. S1***). The results showed that the secondary structures of the two apo forms of dFABP with

different conformational homogeneities varied significantly upon heating (***Fig. 1***). The impact of undesired conformational heterogeneity in dFABP on biophysical analysis was observed in the initial far-UV circular dichroism (CD) spectrum. In contrast to the irreversible profile observed for urea-treated dFABP, there exists a partially reversible profile for GuHCl-purified dFABP after the heating process (***Fig. 1A and B***). In addition, the melting curves obtained at 215 nm revealed that the two apo forms of dFABP behave differently upon interaction with the ligand oleic acid (OA; ***Supp. Fig. S2A***). This result implies that the secondary structures of the urea-treated sample were altered by the heat-induced precipitation of some nonprotein contaminants (***Supp. Fig. S3B and E***) that were absent in the GuHCl-purified sample (***Supp. Fig. S2D, S3F***). The undesired contaminants seem to have high molecular weights, as demonstrated by size-exclusion chromatography (denoted as P1 and A in ***Supp. Fig. S3B***). Despite the small change upon heating observed for the secondary structures of the apo and holo forms in GuHCl-purified dFABP, the melting temperatures measured through intrinsic fluorescence showed that both samples obtained from the two purification methods underwent tertiary structure denaturation (***Supp. Fig. S2C***).

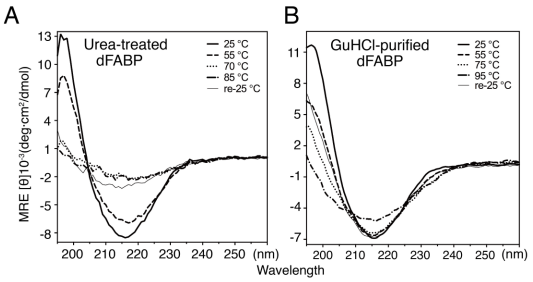

Figure 1. Spectroscopic analysis of urea-treated and GuHCl-purified dFABP. The urea-treated **(A)** and GuHCl-purified **(B)** samples were subjected to far-UV CD spectroscopy for secondary thermal stability analysis. Notably, the reversed 25 °C spectrum (denoted re-25 °C and shown as the thinnest line) in the temperature profile of the urea-treated dFABP was found to be irreversible at 215 nm due to protein precipitation ***(Supp. Fig. S2)***.

Improved conformational homogeneity of dFABP benefits the study of membrane interaction by increasing the proportion of the apo-conformer

The pronounced difference observed in the melting curves of CD spectra convinced us to study the ligand binding based on the dFABP structure with different conformational homogeneities. The HSQC spectrum of the OA complex, holo-dFABP, was assigned (BMRB code 27112, ***Supp. Table S11***) and used as a template spectrum to manually assist the assignments of conformer-A and conformer-B' (a conformer similar to the holo form) in the spectrum of apo-dFABP (BMRB code 27113, ***Supp. Table S12***). Conformer-B' was identified as a liganded-like conformation. The cross-peaks in HSQC spectra indicated a higher proportion of conformer-A in the GuHCl-purified dFABP sample than in the urea-treated sample (***Fig. 2A and B***). Representative residues of conformer-A and conformer-B' showed that the urea-treated apo form of dFABP might be a liganded-like dFABP based on the proportion of conformer-A, which was 3-fold less than that in the GuHCl-purified dFABP on average (***Fig. 2C and D***). Superimposition of the initial and final HSQC spectra upon OA titration revealed that the increasing intensity of conformer-B' in urea-treated dFABP was difficult for comparison to the stoichiometry measured in biochemical assays (***Supp. Fig. S4D***). Although the disappearance of signals in conformer-A was similar to the results observed in GuHCl-purified dFABP (***Supp. Fig. S9***), the larger proportion of conformer-B' in urea-treated dFABP proved to be problematic for subsequent structural analyses on membrane interaction.

Crystallographic structures of dFABP elucidate different potentials for membrane interaction with minimal protein conformational changes

The apo forms of both urea-treated and GuHCl-purified dFABP were crystallized, and their structures were obtained and identified as 5GGE and 5GKB, respectively (***Supp. Table S13***). Unexpectedly, the density maps for the ligand-binding cavity of urea-treated dFABP were incomplete, such that we were uncertain of the liganded state and therefore termed it the liganded-like structure (***Fig. 3A***).

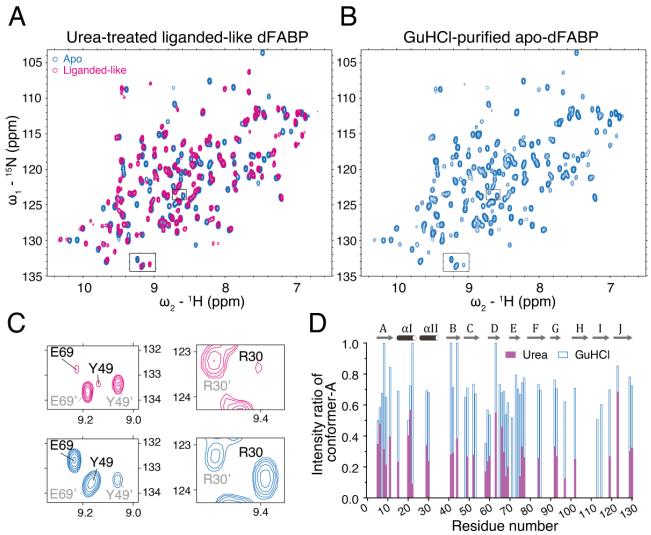

Figure 2. Conformational subpopulations of apo-dFABP determined by HSQC NMR. **(A)** The HSQC spectrum of urea-treated liganded-like dFABP is shown in magenta and is superimposed on that of GuHCl-purified dFABP (light blue). Representative residues for conformer comparison are marked using black boxes. **(B)** The HSQC spectrum of GuHCl-purified apo-dFABP is shown in light blue. Representative residues for conformer comparison are marked using black boxes. **(C)** Representative cross-peaks are enlarged to indicate the different conformational subpopulations in the apo forms of dFABP from the two purification strategies. The residues labelled in grey with the prime symbol represent conformer-B', which is overwhelmingly present in urea-treated liganded-like dFABP, and the dispersion resembles that of OA-liganded holo-dFABP. **(D)** The intensity ratio of conformer-A reveals that the proportion of the apo form is approximately 3 times higher in GuHCl-purified dFABP than in urea-treated dFABP.

Since the region was relatively empty in GuHCl-purified dFABP, containing only three molecules of water, this structure was denoted as apo-dFABP (***Fig. 3B***). The crystal structures presented herein support the importance of conformational homogeneity through the subtle dissimilarities observed between two structures at similar resolution, with different temperature factors observed in the corresponding hypothesized portal (αII, loops of βC-D and βE-F) and gap regions (βD-E). The temperature factor-derived atom distributions of αII and the βC-D loop in the portal region of apo-dFABP were more compact than those in liganded-like dFABP, and those of βE-F in the gap region were expanded during crystallization (***Fig. 3, Supp. Fig. S10***). The larger atom distributions of liganded-like dFABP in the portal region may have resulted from the use of ambiguous restraints for the aliphatic tail of the endogenous unknown ligand, while the internal hydration of water molecules within this region of apo-dFABP may result in more compact atom distributions (***Kaieda and Halle, 2015***). As shown in the 5GGE liganded-like dFABP structure, crystallization might preserve the slow-moving (gap region βE-F) and promiscuous binding (portal region αII) sites where diverse positions occur.

The altered distribution of ordered waters in liganded-like dFABP is worth comparing to that of apo-dFABP. Despite the presence of eleven water molecules within the binding cavity (blue) in both structures, three water molecules (red) were positioned differently (***Fig. 3***). Because of the existence of an unknown ligand, the three differently positioned water molecules were buried in the lower part of the cavity in the liganded-like dFABP but in the upper part of the cavity in apo-dFABP. In contrast to the possibility that the unknown ligand occupied the space in the upper cavity in the liganded-like dFABP, the allosteric ordered waters associated with apo-dFABP may be related to the rearrangement of the hydrogen networks occurring among the surrounding residues, as explained based on a prior molecular dynamics simulation of human heart-type FABP (***Matsuoka et al., 2015***). Residues that are potentially involved in networks with a possible carboxylate group

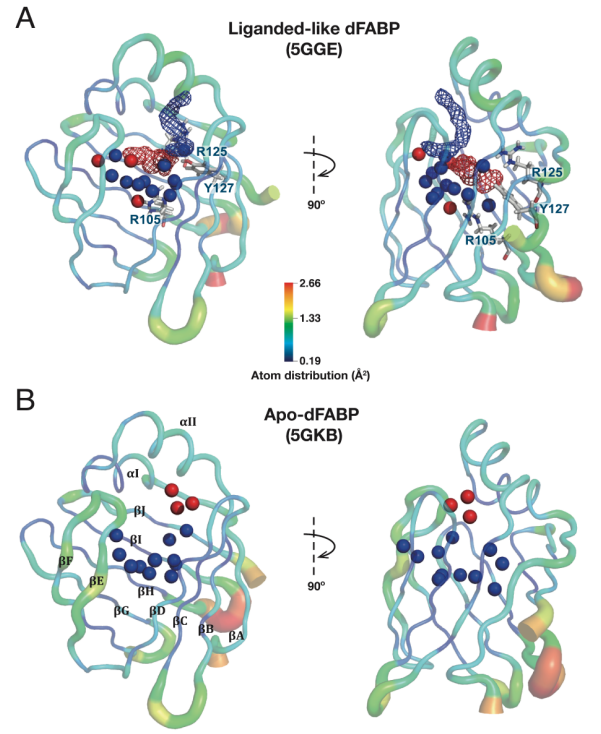

Figure 3. Distribution of water molecules in the apo structures of dFABP. **(A)** Fourteen water molecules within the ligand binding cavity are defined by PyMOL and shown as spheres. Eleven in similar locations are coloured in blue. However, 3 water molecules (shown in red) were observed in different locations in the urea-treated liganded-like dFABP (PDB ID: 5GGE) and the GuHCl-purified apo-dFABP (PDB ID: 5GKB) structures. Both dFABP crystal structures are depicted with the true atom distribution derived from temperature factors, shown in a sausage representation. The discontinuously incomplete electron density maps are shown as red (lower) and blue (upper) meshes. The three residues R105, R125 and Y127, shown as CPK sticks, are within 3.5 Å of the lower part of the unknown ligand-like map and are conserved in FABPs due to their interaction with the carboxylate head of LCFAs. **(B)** The upper part of the cavity in the GuHCl-purified apo-dFABP is filled with 3 water molecules (shown in red) that are located in a different region from those in liganded-like dFABP. Two α-helices are nominated as αI and αII, and the ten β-strands are designated as βA-βJ.

of the unknown ligand (within 3.5 Å) at the bottom of the ligand-binding cavity are also conserved in previous holo-FABP complex structures (***Fig. 3A, 5C***). Accordingly, the distribution of these water molecules ratherthan the unknown ligand near the upper cavity region of apo-dFABP is consistent with the claim of higher conformational homogeneity in the GuHCl-purified dFABP sample.

Membrane interaction reveals a ligand triggering its own unidirectional transport through modulating the dissociation of apo-dFABP from membranes

The GuHCl purification of dFABP enabled a study on the role of conformational relationship in protein–membrane interactions. We first obtained conventional HSQC spectra to observe the discrepancies between the apo and holo forms of GuHCl-purified dFABP through titration with nanodiscs (***Fig. 4A and C***). Next, transverse relaxation-optimized spectroscopy (TROSY) spectra of apo- and holo-dFABP bound to the 1,2-dioleoyl-sn-glycero-3-phospho-(1'-rac-glycerol) (sodium salt) /1,2-dioleoyl-sn-glycero-3-phosphocholine (DOPG/DOPC) lipid nanodiscs (lipid NDs) at a 1:1 molar ratio were acquired to enhance the signal disappearance by virtue of the TROSY effect (***Fig. 4B and D, Supp. Fig. S5A, Supp. Table S14***). Contrary to our expectations, after the addition of the nanodiscs, holo-dFABP exhibited few changes from the previously acquired spectrum (***Fig. 4A***). In contrast, the signals of apo-dFABP in both the HSQC and TROSY spectra were clearly broadened after the addition of nanodiscs, by an order of magnitude after TROSY spectrum, due to a decrease

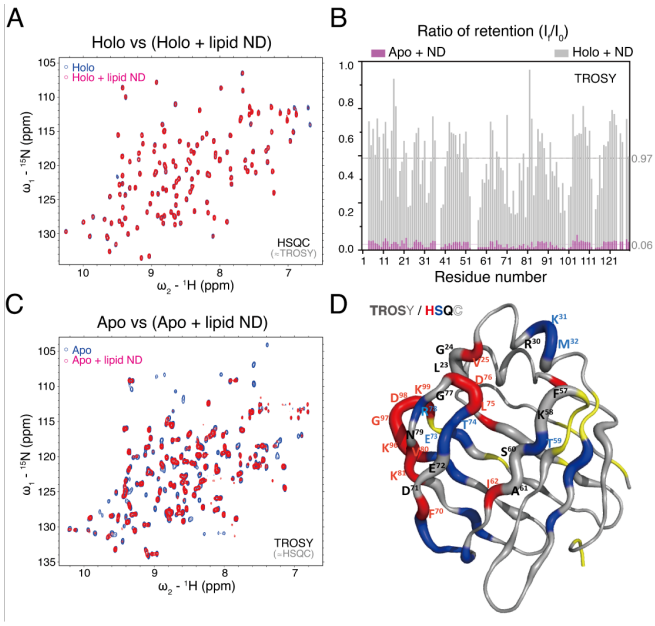

Figure 4. Interaction of GuHCl-purified apo-dFABP (5GKB) with membranes. **(A)** Superimposition of the HSQC spectra of OA-liganded holo-dFABP in the presence (red) or absence (blue) of DOPG/DOPC lipid nanodiscs (ND) at a molar ratio of 1:1. **(B)** The intensity change ratio in the TROSY spectra were obtained by dividing the final intensity (I_f, with ND) by the initial inten mapping onto the apo-dFABP structure (5GKB) corresponds the level of signal disappearance (fraction of attenuation in TRnsity (I_0, without ND). The average difference on TROSY spectra between the two states is approximately 10. **(C)** Superimposition of the HSQC and TROSY spectra of apo-dFABP in the presence (red) or absence (blue) of lipid ND at a molar ratio of 1:1. A similar trend was observed for the representative TROSY spectra shown here. **(D)** The thickness of sausage presentatioOSY spectra) after interacting with lipid NDs. Residues in the αII, βD-F, and βG-H loops and in αI-II (***see Fig. 3B***) with larger changes are labelled, and the unassigned residues are coloured yellow. The thicker segment above the average fraction of attenuation is further divided into three groups according to a serial lipid ND titration (followed using HSQC). Red indicates that the signal decayed immediately, whereas blue indicates that the signal decayed faster than those of the other residues (labelled in black).

in the tumbling rate (***Fig. 4B and C***). This result suggested that apo- rather than holo-dFABP interacts with membrane mimetic nanodiscs. The scale of peak broadening in apo-dFABP in the presence of lipid NDs was plotted as the fraction of attenuation and then superimposed on the tertiary structure of apo-dFABP in a sausage model (***Fig. 4D***).

The diminishing peaks were clustered near the portal and gap regions and near the ligand entry gates (***Fig. 4D, 5B***). This harmony between membrane and ligand interactions enabled the development of a feasible model in which ligand uptake occurs after the attachment of dFABP to membranes near the βG-H loop, and the mechanism involves sliding to the region that encompasses the αII and βD-F regions. To further decipher the enigmatic membrane interaction, residues with attenuation differences above the average value in the TROSY spectra were selected, and their signal decay rates were analysed using HSQC lipid ND titration (***Supp. Fig. S5A and B***). After the integrated evaluation, including signal attenuation and decay rate, four clusters with the following characteristics were defined: 1) signals that decayed more slowly than the average rate (e.g., R30, shown in black); 2) signals that decayed faster than the average rate (e.g., T74, shown in blue); 3) signals that immediately disappeared upon the addition of lipid NDs (e.g., K99, shown in red); and 4) signals that remained detectable (e.g., L51, shown in hollow font) (***Supp. Fig. S5B and C***). The red and blue clusters are also shown in ***Fig. 4D***. More polar and charged residues (namely, D76, R78, K81, K96, D98, and K99), which are responsible for primary membrane attachment, were observed, followed by successive sliding to integrate nonpolar and aromatic residues (namely, L23, G24, V25,

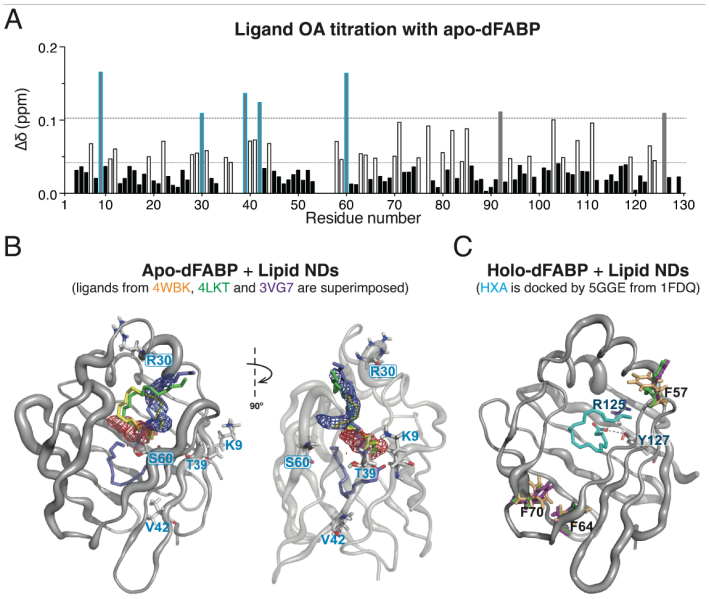

Figure 5. Intersection analysis between ligand binding and membrane interaction. **(A)** The chemical shift perturbations of apo-dFABP were measured by ligand OA titration. Residues with values greater than the total average value (0.04 ppm, the lower, more closely spaced dotted line) were recalculated to obtain an average value similar to that of the upper, more widely spaced dotted line (approximately 0.1 ppm). Five of the seven residues above the highest average CSP value (in blue frames) are found to have higher levels of disappearance (fraction of attenuation in TROSY spectra) during lipid ND interaction. **(B)** B. The effect of lipid NDs on apo-dFABP mapping onto the apo-dFABP structure (5GKB) is shown in sausage representation. The five residues with higher levels of disappearance during lipid ND interaction are shown as sticks and are labelled on the structure; two of these (in squares) are located in the membrane-associated region. The maps of the unknown ligand in liganded-like dFABP (5GGE, red and blue meshes), stearic acid of human heart-type FABP (4WBK, yellow sticks), arachidonic acid of human epidermal-type FABP (4LKT, green sticks) and palmitic acid in human liver-type FABP (3VG7, purple sticks) are shown using the PyMOL structure alignment suit for ligand orientation comparison. **(C)** The effect of lipid NDs on holo-dFABP mapping onto the liganded-like structure (5GGE) is shown in sausage representation. The structure is superimposed with the 5GGE docking ligand using docosahexanoic acid (HXA, cyan sticks) in human B-FABP (1FDQ) and PatchDock, and the two residues interacting with the carboxylate head group of the docked HXA ligand are indicated in CPK with labels. Three aromatic residues of 5GGE, 5GKB and the docking model, which are located in the βC-D loop and βD-E, are labelled in magenta, green and mustard, respectively.

F57, and A61) in the portal and gap regions. Polar residues can be reasonably inferred to engage the polar heads of biomembranes and nonpolar residues to interact with hydrophobic ligands embedded in lipid bilayers. This interplay of membrane–association regions constructed in space is likely to imitate amphitropic peripheral proteins.

A ligand rescue experiment was performed using OA for further analyses of the cross-peak change, and representative residues participating in the membrane interaction are shown in ***Supp. Fig. S6***. Notably, the signals representing apo-dFABP binding to nanodiscs recovered by rescued ligand OA were more similar for conformer-B', which did not completely superimpose on the spectra of OA-liganded holo-dFABP, implying that the ligand can be internalized into the escort protein and modulate the dissociation of the holo form from the membrane mimetics. In relation to both ligand binding and membrane interaction, four out of five selected residues shown in ***Fig. 5B*** are polar and charged, and the two residues in squares (R30 and S60) lie at the protein–membrane interface. The unknown ligand map coheres with those of ligands from other similar escort proteins (e.g., heart-type FABP, epidermal-type FABP and liver-type FABP), and the docking complex signifies that the aliphatic tails of ligands around the portal region interfere with the protein–membrane interactions (***Fig. 5C***).

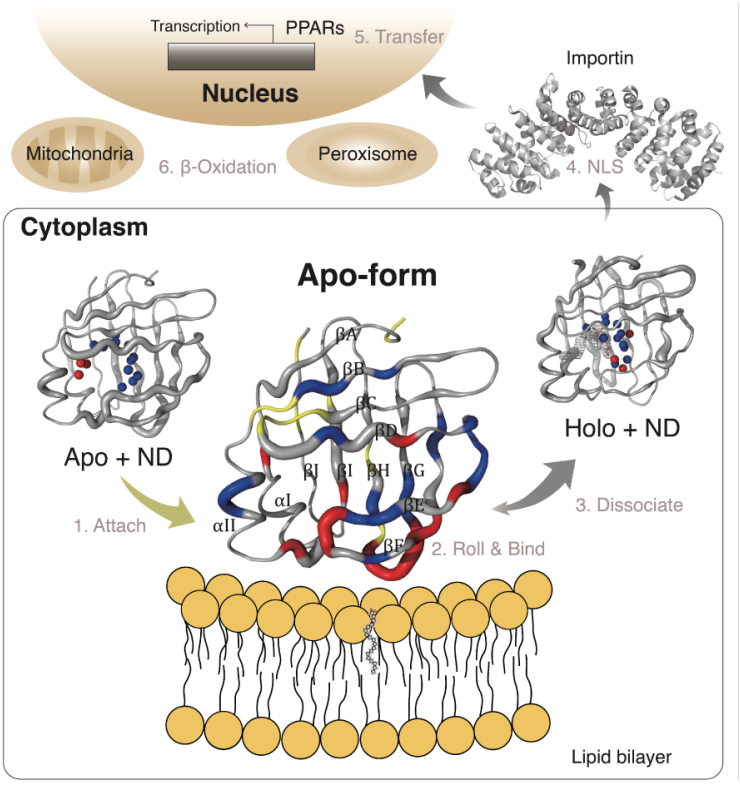

Figure 6. Proposed model for ligand-regulated dFABP transport. The mechanistic trafficking model of fatty acid (FA) accompanied by dFABP is shown in detail. A putative ligand transfer model was proposed in conjunction with our study (as shown in the square) as follows: 1) The apo form of the escort protein FABP attaches to the lipid bilayer. 2) Apo-FABP slides to accommodate complementary LCFAs. 3) The ligand-bound form, holo-FABP, dissociates from the lipid bilayer. 4) Importin α (PDBID: 1EJL) recognizes the spatial arrangement of the NLS in the holo form of FABPs (***Amber-Vitos et al., 2015***). 5) Holo-FABP transfers the ligand to PPARs (***Armstrong et al., 2014***). 6) PPARs trigger gene transcription and produce proteins for lipid metabolism (e.g., β-oxidation) in the mitochondria or through other signaling pathways. The fraction of attenuation is illustrated in sausage representation for apo- and holo-dFABP (***Fig. 4D, Supp. Table S14***) (5GKB and 5GGE, respectively), and the PyMOL-defined cavity water molecules and incomplete ligand-like maps are shown in spheres and meshes, respectively.

According to comprehensive data obtained for these residues, when the apo-dFABP first approaches a lipid ND, a rolling motion occurs in the region composing theβG-HβE-F loops and the αI-II turn, which subsequently turns towards the portal and gap regions for ligand accommodation (***Fig. 6***). In particular, the intensity of conformer-B' remained almost unchanged during lipid ND titration, whereas that of conformer-A of apo-dFABP continued to diminish (***Supp. Fig. S6B and S7C***). Together with the consistent results showing a barely changed intensity in conformer-B' between apo-dFABP and holo-dFABP during lipid ND interaction, these findings strongly indicate that the ligands escorted by dFABP would favour unidirectional transportation (***Fig. 4A and B***).

Discussion

Intracellular cargo transport is a complex and highly dynamic process. By analysing dFABP with enriched conformational homogeneity, we present a mechanistic model for the transport directionality of lipophilic cargo molecules in representative escort proteins, namely, FABPs. FABPs comprise ten β strands, which are organized orthogonally as a clamp appended to a short helix-turn-helix motif as the portal cap region near N terminus (***Storch and Thumser, 2010***). Previous studies have reported that the minor open state of the portal region in apo forms of FABPs was responsible for

ligand entry (***Hodsdon and Cistola, 1997; Yu and Yang, 2016***), while the slow protein conformational exchange was suggested to be irrelevant to the ligand association (***Xiao et al., 2016***). A fundamental problem with escort protein-dependent ligand transport, such as the transport of LCFAs by FABPs, is whether the directionality is reversible or irreversible. Initial analysis of the ligand–FABP complex structures in the Protein Data Bank did not reach any conclusion regarding the transport mechanism (***LiCata and Bernlohr, 1998***), and the hypothesis that the inward state of the conserved Phe residue in the βC-D loop of FABPs corresponds to the liganded closed form and the outward state to the unliganded open form has not been universally consistent (e.g., 5BVQ, 4I3B). In our view, the potential interactions among several key factors, including the escort protein, the target ligand, and the ligand donor, all need to be considered concurrently for a successful interpretation of the dynamic cargo transport mechanism.

In this article, we provide several lines of compelling evidence, including biophysical analyses and structural comparisons, to support our speculation that the lipophilic ligand facilitates protein–ligand complex dissociation from ligand donor membranes. The level of trace contaminants in the urea-treated sample was unproblematic in our conventional ligand-protein interaction analyses (***Supp. Fig. S4B and C, Supp. Fig. S8***). According to the CD studies shown in ***Fig. 1*** and ***Supp. Fig. S2***, however, some biophysical properties such as thermal stability might yield inappropriate interpretations (***Zhang et al., 1992; Tsukamoto et al., 2009***). The decreased Tm of the urea-treated sample in CD experiments might have resulted from an association between the protein and nonprotein membrane-like debris (***Supp. Fig. S3***). The differences between the apo and holo forms of urea-treated dFABP that are seen in far-UV CD spectra may result from the presence of associated impurity because both forms had secondary structures with similar thermal stability in the GuHCl-purified sample (***Supp. Fig. S2A***). Further investigation of the membrane interactions confirmed that the holo form had far fewer interactions with membrane mimetics (***Fig. 4A and B***) and that the apo form dissociated from membranes by an additional ligand binding, as seen in the rescue study (***Supp. Fig. S6C***). Therefore, the ability of OA to cause the urea-treated sample to dissociate from membrane-like debris and adopt the free OA-liganded form would explain the higher secondary thermal stability of the OA-liganded urea-treated dFABP (***Supp. Fig. S2A***). Although the analysis of protein thermal stability based on precipitation using far-UV CD spectra was not applicable (***Supp. Fig. S2A and D***), the proteins unfolded cooperatively and globally, as seen in intrinsic fluorescence experiments (***Supp. Fig. S2C***). The changes in Tm (as determined using intrinsic fluorescence spectra) between the apo and holo forms of urea-treated and GuHCl-purified dFABP were approximately 10 °C and 5 °C, respectively, and both holo forms had identical melting curves, suggesting that the liganded forms of dFABP were consistent (***Supp. Fig. S2C***). Moreover, the difference in stability between the apo and holo forms was confirmed by a chemical denaturation experiment, which showed that the rigidity assisted by the ligand was similar to the thermal stability (***Supp. Fig. S4A***). Altogether, the intrinsic fluorescence experiments on dFABP demonstrated that the findings regarding the difference in thermal unfolding between the apo and holo forms were consistent with those of previous CD studies (***Gericke et al., 1997; Tsukamoto et al., 2009***), even if the Tm values from the CD spectra were not readily interpreted.

We discovered through both microscopic and macroscopic analyses that the general heterogeneity of FABPs, including unknown ligands and membrane-like debris, may be a reason for inconsistency in the Phe residue orientation in the βC-D loop (e.g., penguin apo-AFABP, 5BVQ). Based on the crystallization results, the urea-treated liganded-like dFABP exhibited a tertiary structure similar to that of the GuHCl-purified apo-dFABP, except that no ligand-like electron density was calculated inside its binding cavity (***Fig. 3***). Therefore, the difference in temperature factors around the portal and gap regions may be attributed to conformational heterogeneity (***Supp. Fig. S10***). On the basis of a further comparison of the ordered waters in the ligand binding cavity of liganded-like and apo-dFABPs, we conjectured that the residues around ligand entry sites likely have higher temperature factors in the apo form of urea-treated dFABP because of the possible lack of an ordered-water hydrogen networks resulting from the flexible hydrophobic tail of the

unknown ligand (***Fig. 3A***). Although the HSQC spectrum of urea-treated liganded-like dFABP exhibited minor perturbation upon ligand binding (***Supp. Fig. S9A***), a high proportion of the holo form left inadequate space for further membrane interaction. The spectra of urea-treated liganded-like dFABP and OA-dFABP, especially in the region from βD to E, are indistinguishable from ligand entry to membrane interaction (***Fig. 2D and 4D***).

Consequently, GuHCl-purified apo-dFABP was used to study the relationship between proteins and membranes in the presence and absence of ligands. The broadened apo-dFABP signals resulting from membrane interaction were superimposed on the unliganded 5GKB structure, and the residues were grouped by decay features corresponding to the order of membrane attachment (***Fig. 4D, Supp. Fig. S5***). By carefully dissecting the clusters in terms of ligand binding and membrane interaction, a harmonious coupling was found to explain the interactions among lipophilic ligands, escort proteins, and bilayer membranes as follows: 1) based on the crystallographic temperature factors, we assumed that βE-F controls ligand entry; and 2) membrane attachment was described as being initiated by attaching to the βG-H loop and rolling towards the region involving the αII and βD-E because the signals for the βG-H and βE-F loops decayed faster than those for the portal and gap regions (αII/βD-E) (***Fig. 6***). The ligand is assumed to participate in the interface between the protein and the membrane, and liganded dFABP tended to dissociate from the membranes after binding to the ligand, as reported by ligand OA rescue analysis (***Supp. Fig. S5***).

Numerous studies have suggested that positively charged residues in the helix region control membrane interactions (***Herr et al., 1996; Tsfadia et al., 2007; Dyszy et al., 2013***). More recent research has demonstrated that these residues are part of a spatially arranged nuclear leading sequence (***Ayers et al., 2007; Gillilan et al., 2007; Armstrong et al., 2014***). Although residues in αII, such as R30, were disturbed by ligand and membrane titration (***Supp. Fig. S6A and B***), they were neither the main cause of nor independent contributors to the membrane attachment. In addition to allowing further study of membrane interaction, the enriched conformational homogeneity of dFABP provides a promising means of distinguishing membrane interactions from other interactions and demonstrates that the conformer-A signals of residues that participate in membrane interaction tend to disappear when the interaction occurs (***Supp. Fig. S6B, S7C***). Residues that do not strongly contribute to membrane interaction and those facing the ligand binding cavity (e.g., Y127) do not fully lose intensity or show no chemical shift perturbation after membrane titration (***Supp. Fig. S7D***), in contrast to how ligand titration transforms conformer-A into the OA-liganded holo form (***Supp. Fig. S7B***).

According to our findings, the greatly decreased membrane affinity of liganded dFABP determines ligand transport directionality. Not only does the orientation of ligand binding inside the protein affect repulsion in the protein–membrane interaction (***Fig. 7B and C***), but also the ligand donor membranes may induce the open state of the escort protein to enable ligand uptake (***Yu and Yang, 2016***). Considering that lipophilic LCFAs are physiologically embedded in membranes and that high affinity for FABPs is observed in vitro, the combination of these two scenarios may further explain why not all ligands with similar binding affinities can trigger FABP nuclear translocation. First, ligands that can be uploaded complementarily into the escort protein may repel either the αII of FABPs (***Cistola et al., 1996***) or the charged interface of FABP–membrane due to their aliphatic tails and thereby force FABPs to dissociate from the membrane (***Fig. 5***). In contrast, ligands that do not fold properly into the binding cavity of FABPs would leave a tail below the membrane surface inside the hydrophobic environment, thus preventing the protein from dissociating. Moreover, the spatial distribution of charged residues in βC-F and the conserved Phe residue in the βC-D loop seems to facilitate the attachment of FABPs to membranes. These findings might be crucial, necessitating the re-evaluation of previous studies on the interactions among FABPs, complementary ligands and membranes based on molecular dynamic simulations, which have mostly focused on explaining how LCFAs enter FABPs or how holo-FABPs transport ligands to membranes (***Friedman et al., 2006; Zamarreno et al., 2012; Ragona et al., 2014***). The relationship between liganded FABPs and membranes provides an alternative interpretation: only through a specific orientation of the

ligand in the protein can the aliphatic tail modulate protein–membrane dissociation and act as activator ligands to control protein–ligand complex release for nucleocytoplasmic translocation (***Armstrong et al., 2014***). The use of blockers targeting holo-FABPs instead of competitors for apo-FABPs may be able to interrupt the pathways for entering the nucleus or for interacting with effectors. Through illuminating the unidirectional transport by dFABP, this study advances research on FABPs, particularly on their relationships with complementary LCFAs and membranes, which will enable further investigation of their roles in the nucleus. The mechanism generalizes a model, obtained by clarifying the working patterns of FABPs, in which the complementary lipophilic ligand is the decisive factor in regulating its own transport directionality in membrane-associated escort proteins.

Materials and Methods

Cloning and expression of dFABP

The second spliced isoform (CG6783-B) of the dFABP locus (CG6783) in the *Drosophila* genome was found to share the highest homology to mammalian brain-type FABP, and its 130-residue peptide sequence was expressed and purified for subsequent structural studies (***Gerstner et al., 2011b***). In brief, the open reading frame coding for dFABP isoform B was chemically synthesized with E. coli-optimized codons (Eurofins Scientific, Luxembourg), and inserted into the pET23a(+) expression vector (Merck, Darmstadt, Germany) at the NdeI/XhoI sites. The dFABP-pET23a plasmid was subsequently transformed into E. coli BL21-Gold (DE3) competent cells (Thermo Fisher Scientific, MA, USA) for recombinant protein expression. Individual colonies were selected, and an aliquot of host cells harbouring the correct insert was inoculated into 20 mL of Luria broth (LB) containing 100 μg/mL ampicillin. The broth was incubated at 37 °C with 180 rpm agitation for 12 h as a condensed starting culture. The 20-mL cell culture was either poured into 800 mL of LB or precipitated and then resuspended in 1 L of uniformly isotopes-labelled M9 medium, which consisted of 1 g of ^{13}C-glucose/1 g ^{15}N- NH_4Cl (Cambridge Isotopes Laboratories, MA, USA) with 20 μg/mL ampicillin. Subsequently, dFABP expression was induced with 0.2 mM isopropyl β-D-1-thio-galactopyranoside (IPTG) when the optical density at 600 nm reached 0.6, and the cultures were incubated for an additional 6 h at 37 °C.

Purification of dFABP with higher conformational homogeneity

Supp. Fig. S1 represents the flowchart for dFABP purification, by our improved new strategy with the combination of 8 M urea and the partially unfolding reagent 2 M GuHCl, depending on the denaturation analysis (***Supp. Fig. S4A***). Briefly, a batch of 800 mL LB broth or 1 L isotopes-labelled of the protein expression culture was harvested by 12,000 × *g* centrifugation at 4 °C for 20 min. Cell pellets were resuspended collectively in 30 mL of lysis buffer (20 mM Tris pH 8.0, 2 mM EDTA, 1 mM β-ME, 0.05% NaN_3) and frozen at -20 °C before further purification. The thawed cells were lysed by sonication and centrifuged at 38,500 × *g* for 15 min at 4 °C. The pellet was solubilized in 5 mL of 8 M urea at 4 °C for 3 h and then centrifuged again at 38,500 × *g* at 4 °C for 15 min to remove insoluble debris. The supernatant was dialyzed against 1 L of the sample buffer (20 mM Tris and 1 mM β-ME, pH 8.0) using 3-kDa molecular weight cutoff dialysis tubing (Orange Scientific, Braine-l'Alleud, Belgium) and stirred at 4 °C for 6 h. The precipitates were removed by centrifugation at 38,500 × *g* at 4 °C for 15 min, and the supernatant was mixed with an equal volume of buffer B (1 M $(NH_4)_2SO_4$ in 20 mM Tris, pH 8.0) and concentrated to 10 mL for hydrophobic interaction chromatography (5-mL HiTrap phenyl HP column, GE Healthcare, IL, USA). Subsequently, a 2-mL elution of hydrophilic flow-through was incubated in the absence (denoted as urea-treated dFABP) or presence (denoted as GuHCl-purified dFABP) of 2 M GuHCl preincubated at room temperature for 30 min for the next size-exclusion chromatography. The urea-treated dFABP was obtained and validated by twice injection of S-200 size-exclusion chromatography (HiPrep 16/60 Sephacry S-200 HR, GE Healthcare), and the GuHCl-purified dFABP underwent two rounds of S-200 size-

exclusion chromatography, with final validation by S-75 size-exclusion chromatography (Superdex 75 10/300 GL, GE Healthcare). All chromatography samples had a volume of 5 mL after the removal of precipitates by 0.22-μm membrane filters. The crude quality of the desired dFABP protein after each step was assessed using SDS-PAGE. The polished samples at the final purification step were further determined through ESI UPLC Q-TOF mass spectrometry (Impact HD, Bruker, MA, USA) and the yield of 1 L of culture was approximately 15 mg, as measured by Bradford and BCA assays. The final dFABP samples were stored in 500 μM in the sample buffer at 4 °C until use in 6 months.

Spectroscopic characterization of dFABP

A 25-μM sample was prepared in sample buffer using 0.1-cm quartz cuvette for an Aviv Model 202 CD spectrometer (Aviv Biomedical, NJ, USA) and a 2-μM sample was used for intrinsic fluorescence measurement (F-7000, HITACHI, Tokyo, Japan). The mean residue ellipticity (MRE) was calculated based on the initial sample concentration in temperature-dependent far-UV CD experiments. As a result of the decrease in soluble concentration during the heating process in the urea-treated sample, the CD melting curves from 25 °C to 95 °C measured at a wavelength of 215 nm were expressed in millidegrees instead of MRE. Holo-dFABP was combined with OA (100 mM stock in 250 mM KOH, Avanti Polar Lipids, AL, USA) to achieve a molar ratio of 1:2 in the CD and fluorescence spectroscopic experiments. The excitation wavelength of intrinsic fluorescence was set at 275 nm because there were four tyrosines instead of tryptophan in the dFABP sequence and detected at an emission wavelength of 303 nm. Each temperature of the stepwise melting experiments was equilibrated for 10 s before manual detection. The CD melting curve was automatically set at increments of 2 °C from 24 °C to 96 °C and equilibrated for 1 s with 0.5-s data averaging. The assay results were fitted using the Sigmoidal model in GraphPad Prism 6 software (GraphPad Software, Inc. La Jolla, CA, USA).

Crystallographic characterization of dFABP

The dFABP samples were concentrated to approximately 8 mg/mL in 20 mM Tris buffer (pH 8.0) for crystallization. Crystals were screened either manually or by using the automatic protein crystallization robot Oryx8 (Douglas Instruments, Hungerford, UK) with Wizard crystallization screens (Rigaku, WA, USA). The urea-treated dFABP (denoted as 5GGE) was crystallized through vapour diffusion in hanging-drop format, and a 1-μL protein sample was mixed with a 1-μL drop of reservoir solution against 200 μL of reservoir solution in 24-well Linbro plates (Flow Laboratories, VA, USA). The GuHCl-purified dFABP (denoted as 5GKB) was crystallized through vapour diffusion in sitting-drop format. The microbatch screening system was applied under the crystallization conditions of Emerald Wizard II-F7 (0.1 M phosphate citrate, 1.6 M NaH_2PO_4/0.4 M K_2HPO_4, final pH 5.2), and 0.3 μL of GuHCl-purified dFABP was mixed with 0.3 μL of reservoir solution against 60 μL of crystallization solution in 96-well crystallization plates. To acquire X-ray diffraction data, crystals were grown for 2 months at 20 °C, and data acquisition was performed at the National Synchrotron Radiation Research Center, Taiwan. The data were processed and scaled using HKL2000 software, and the molecular replacement program MOLREP in CCP4 was applied for phase determination (***Winn et al., 2011***). The initial models for 5GGE and 5GKB were 1FTP and 5GGE, respectively. Further model building, the incorporation of the ligand citrate in 5GGE, and both structural refinements were performed using the PHENIX suite (***Moriarty et al., 2009***). The structure of liganded-like dFABP (5GGE) was subjected to the docking program PatchDock for ligand docking (docosahexanoic acid, HXA of 1FDQ).

NMR HSQC spectroscopy analysis

Samples for NMR were buffer exchanged into 50 mM phosphate buffer (pH 6.8) with the addition of 10% D_2O and trace 4,4-dimethyl-4-silapentane-1-sulfonate as a calibration standard for spectra collected at 298K. An Avance-600 MHz spectrometer was used for the OA titration of HSQC spectra, and an Avance-850 MHz spectrometer (Bruker, Germany) equipped with a cryoprobe was used

to acquire the spectra for nanodisc interactions. The holo form of the OA-dFABP sample was prepared at a 1:3 molar ratio of protein to OA, and the 3D spectra (HNCA, HNCOCA, HNCACB, CBCACONH, HNCO and HNCACO) for sequential assignments were acquired on the Avance-850 MHz instrument. Identical 3D NMR experiments for assignments of apo-dFABP were recorded for back-calculation from the OA-dFABP assignments (Supp. Table S11, S12). The data were processed using NMRPipe (***Delaglio et al., 1995***) and autoassigned by MANI PINE server v.2.0 (***Bahrami et al., 2009***), with manual inspection through NMR assignment and Sparky integration software (Goddard TD & Kneller DG, 2008, SPARKY 3. University of California, San Francisco, CA, USA). Chemical shift perturbations (CSPs) from the initial conformer-A to the final holo form for dFABP were analysed by weighting the averaged ^{1}H and ^{15}N chemical shift changes with the equation $\triangle\delta = [(\triangle\delta_{1HN})^2 + (0.17\triangle\delta_{15N})^2]^{1/2}$.

Acknowledgements

We thank the Biological Crystallography Faculty of National Synchrotron Radiation Research Center (Taipei, Taiwan) for technical supports and assistance in the X-ray and data collection. We are grateful to Dr. Tsyr-Yan Dharma Yu and Mr. Julien Massiot of the Institute of Atomic and Molecular Sciences at Academia Sinica (Taipei, Taiwan) for constructive guidance on TROSY experiments and kind preparation of lipid nanodiscs. We appreciate Dr. Yet-Ran Chen of the Agricultural Biotechnology Research Center at Academia Sinica (Taipei, Taiwan) for valuable comments on mass spectra and lipidome experiments. We are indebted to Drs. Lee-Wei Yang and Shih-Che Sue of the Institute of Bioinformatics and Structural Biology at National Tsing Hua University (Hsinchu, Taiwan), and Dr. Shang-Te Danny Hsu of the Institute of Biological Chemistry at Academia Sinica (Taipei, Taiwan) for their insightful remarks and helpful suggestions on this project. We are also thankful to Dr. Yi-Zong Lee and Mr. Liang-Yuan Chiu of the Institute of Bioinformatics and Structural Biology at National Tsing Hua University (Hsinchu, Taiwan) for their kind assistance with 3D NMR spectra. This research was supported by grants from Ministry of Science and Technology (MOST106-2319-B-400-001; MOST105-2311-B-007-002 & MOST103-2325-B-400-002) and National Health Research Institute (CA-103-PP-13; CA-104-PP-13 & CA-105-PP-13), Taiwan.

Additional information

Author contributions

Y.Y.C. designed the study, executed all experimental work, data interpretation and drafted the manuscript. Y.F.H. collaborated in improving the protein purification processes. H.H.L. contributed to cloning and crystal collection of urea-treated wild-type dFABP. W.S.C. and P.C.L. contributed to project supervision and assisted manuscript preparation.

Competing interests

The authors declare that no competing interests exist.

Reference

Amber-Vitos O, Kucherenko N, Nachliel E, Gutman M, Tsfadia Y. 2015. The interaction of FABP with kapα. PLoS One 10:e0132138. DOI: 10.1371/journal.pone.0132138, PMID: 26284534

Anthony TE, Mason HA, Gridley T, Fishell G, Heintz N. 2005. Brain lipid-binding protein is a direct target of Notch signaling in radial glial cells. Gene Dev 19:1028-1033. DOI: 10.1101/gad.1302105, PMID: 15879553

Armstrong EH, Goswami D, Griffin PR, Noy N, Ortlund EA. 2014. Structural basis for ligand regulation of the fatty acid-binding protein 5, peroxisome proliferator-activated receptor β/δ (FABP5-PPAR β/δ) signaling pathway. J Biol Chem 289:14941-14954. DOI: 10.1074/jbc.M113.514646, PMID: 24692551

Ayers SD, Nedrow KL, Gillilan RE, Noy N. 2007. Continuous nucleocytoplasmic shuttling underlies

transcriptional activation of PPARγ by FABP4. Biochemistry 46:6744-6752. DOI: 10.1021/bi700047a, PMID: 17516629

Bahrami A, Assadi AH, Markley JL, Eghbalnia HR. 2009. Probabilistic interaction network of evidence algorithm and its application to complete labeling of peak lists from protein NMR spectroscopy. PLoS Comput Biol 5:e1000307. DOI: 10.1371/journal.pcbi.1000307, PMID: 19282963

Bayburt TH, Grinkova YV, Sligar SG. 2002. Self-assembly of discoidal phospholipid bilayer nanoparticles with membrane scaffold proteins. Nano Lett 2:853-856. DOI: 10.1021/nl025623k, PMID: 14573860

Bazinet RP, Layé S. 2014. Polyunsaturated fatty acids and their metabolites in brain function and disease. Nat Rev Neurosci 15:771-785. DOI: 10.1038/nrn3820, PMID: 25387473

Boden G. 2008. Obesity and free fatty acids (FFA). Endocrin Metab Clin 37:635-646. DOI: 10.1016/j.ecl.2008.06.007, PMID: 18775356

Ceccon A, D'Onofrio M, Zanzoni S, Longo DL, Aime S, Molinari H, Assfalg M. 2013. NMR investigation of the equilibrium partitioning of a water-soluble bile salt protein carrier to phospholipid vesicles. Proteins: Struct Funct Bioinf 81:1776-1791. DOI: 10.1002/prot.24329, PMID: 23760740

Cistola DP, Kim K, Rogl H, Frieden C. 1996. Fatty acid interactions with a helix-less variant of intestinal fatty acid-binding protein. Biochemistry 35:7559-7565. DOI: 10.1021/Bi952912x, PMID: 8652536

Corsico B, Cistola DP, Frieden C, Storch J. 1998. The helical domain of intestinal fatty acid binding protein is critical for collisional transfer of fatty acids to phospholipid membranes. Proc Natl Acad Sci USA 95:12174-12178. DOI: https://doi.org/10.1073/pnas.95.21.12174, PMID: 9770459

Delaglio F, Grzesiek S, Vuister GW, Zhu G, Pfeifer J, Bax A. 1995. NMRPipe: a multidimensional spectral processing system based on UNIX pipes. J Biomol NMR 6:277-293. DOI: 10.1007/BF00197809, PMID:8520220

Dyszy F, Pinto APA, Araújo APU, Costa AJ. 2013. Probing the interaction of brain fatty acid binding protein (B-FABP) with model membranes. PLoS One 8. DOI: 10.1371/journal.pone.0060198, PMID: 23555925

Flower DR. 1996. The lipocalin protein family: structure and function. Biochemical J 318:1-14. DOI: 10.1042/bj3180001, PMID: 8761444

Friedman R, Nachliel E, Gutman M. 2006. Fatty acid binding proteins: same structure but different binding mechanisms? Molecular dynamics simulations of intestinal fatty acid binding protein. Biophy J 90:1535-1545. DOI: 10.1529/biophysj.105.071571, PMID: 1367305

Furuhashi M, Hotamisligil GS. 2008. Fatty acid-binding proteins: role in metabolic diseases and potential as drug targets. Nat Rev Drug Discov 7:489-503. DOI: 10.1038/nrd2589, PMID: 18511927

Gericke A, Smith ER, Moore DJ, Mendelsohn R, Storch J. 1997. Adipocyte fatty acid-binding protein: interaction with phospholipid membranes and thermal stability studied by FTIR spectroscopy. Biochemistry 36:8311-8317. DOI: 10.1021/bi970679s, PMID: 9204877

Gerstner JR, Vanderheyden WM, Shaw PJ, Landry CF, Yin JC. 2011a. Cytoplasmic to nuclear localization of fatty-acid binding protein correlates with specific forms of long-term memory in Drosophila. Commun Integr Biol 4:623-626. DOI: 10.4161/cib.4.5.16927, PMID: 22046481

Gerstner JR, Vanderheyden WM, Shaw PJ, Landry CF, Yin JCP. 2011b. Fatty-acid binding proteins modulate sleep and enhance long-term memory consolidation in Drosophila. PLoS One 6. DOI: 10.1371/journal.pone.0015890, PMID: 21298037

Gillilan RE, Ayers SD, Noy N. 2007. Structural basis for activation of fatty acid-binding protein 4. J Mol Biol 372:1246-1260. DOI: 10.1016/j.jmb.2007.07.040, PMID: 17761196

Glatz JFC, van der Vusse GJ. 1996. Cellular fatty acid-binding proteins: their function and physiological significance. Prog Lipid Res 35:243-282. DOI: https://doi.org/10.1016/S0163-7827(96)00006-9, PMID: 9082452

Guariento M, Assfalg M, Zanzoni S, Fessas D, Longhi R, Molinari H. 2009. Chicken ileal bile-acid-binding protein: A promising target of investigation to understand binding co-operativity across the protein family. Biochemical J 425:413-424. DOI: 10.1042/BJ20091209, PMID: 19874274

He Y, Yang X, Wang H, Estephan R, Francis F, Kodukula S, Storch J, Stark RE. 2007. Solution-state molecular structure of apo and oleate-liganded liver fatty acid-binding protein. Biochemistry 46:12543-12556. DOI: 10.1021/bi701092r, PMID: 17927211

Herr FM, Aronson J, Storch J. 1996. Role of portal region lysine residues in electrostatic interactions between heart fatty acid binding protein and phospholipid membranes. Biochemistry 35:1296-1303. DOI: 10.1021/Bi952 204b, PMID: 8573586

Herrmann JM, Malkus P, Schekman R. 1999. Out of the ER — outfitters, escorts and guides. Trends Cell Biol 9:5-7. DOI: https://doi.org/10.1016/S0962-8924 (98)01414-7, PMID: 10087610

Hertzel AV, Bernlohr DA. 2000. The mammalian fatty acid-binding protein multigene family: molecular and genetic insights into function. Trends Endocrin Metab 11:175-180. DOI: https://doi.org/10.1016/S1043-2760(00) 00257-5, PMID: 10856918

Hodsdon ME, Cistola DP. 1997. Discrete backbone disorder in the nuclear magnetic resonance structure of apo intestinal fatty acid-binding protein: implications for the mechanism of ligand entry. Biochemistry 36:1450-1460. DOI: 10.1021/Bi961890r, PMID: 9063893

Hotamisligil GS, Bernlohr DA. 2015. Metabolic functions of FABPs — mechanisms and therapeutic implications. Nat Rev Endocrinol 11:592-605. DOI: 10.1038/nrendo.2015.122, PMID: 26260145

Kaieda S, Halle B. 2015. Time scales of conformational gating in a lipid-binding protein. J Phys Chem B 119:7957-7967. DOI: 10.1021/acs.jpcb.5b03214, PMID: 26012957

Kim HK, Storch J. 1992. Free fatty acid transfer from rat liver fatty acid-binding protein to phospholipid vesicles: effect of ligand and solution properties. J Biol Chem 267:77-82. DOI: 10.1194/jlr.M500140-JLR200, PMID: 1730626

LiCata VJ, Bernlohr DA. 1998. Surface properties of adipocyte lipid-binding protein: response to lipid binding, and comparison with homologous proteins. Proteins: Struct Funct Genet 33:577-589. DOI: https://doi.org /10.1002/(SICI)1097-0134(19981201)33:4<577::AID-PROT10>3.0.CO;2-2, PMID: 9849941

Lücke C, Zhang FL, Rüterjans H, Hamilton JA, Sacchettini JC. 1996. Flexibility is a likely determinant of binding specificity in the case of ileal lipid binding protein. Structure 4:785-800. DOI: https://doi.org/10.1016/S0969-2126(96) 00086-X, PMID: 8805562

Marinelli F, Kuhlmann SI, Grell E, Kunte HJ, Ziegler C, Faraldo-Gómez JD. 2011. Evidence for an allosteric mechanism of substrate release from membrane-transporter accessory binding proteins. Proc Natl Acad Sci USA 108:E1285-E1292. DOI: 10.1073/pnas.1112534108, PMID: 22084072

Matsuoka D, Sugiyama S, Murata M, Matsuoka S. 2015. Molecular dynamics simulations of heart-type fatty acid binding protein in apo and holo forms, and hydration structure analyses in the binding cavity. J Phys Chem B 119:114-127. DOI: 10.1021/jp510384f, PMID: 25489786

Michalik L, Desvergne B, Wahli W. 2004. Peroxisome-proliferator-activated receptors and cancers: complex stories. Nat Rev Cancer 4:61-70. DOI: 10.1038/nrc1254, PMID: 14708026

Moriarty NW, Grosse-Kunstleve RW, Adams PD. 2009. Electronic ligand builder and optimization workbench (eLBOW): a tool for ligand coordinate and restraint generation. Acta Crystallogr D Biol Crystallogr 65:1074-1080. DOI: 10.1107/S0907444909029436, PMID: 19770504

Noy N. 2007. Ligand specificity of nuclear hormone receptors: sifting through promiscuity. Biochemistry 46:13461-13467. DOI: 10.1021/bi7018699, PMID: 17983246

Pervushin K, Riek R, Wider G, Wüthrich K. 1997. Attenuated T-2 relaxation by mutual cancellation of dipole-dipole coupling and chemical shift anisotropy indicates an avenue to NMR structures of very large biological macromolecules in solution. Proc Natl Acad Sci USA 94:12366-12371. DOI: https://doi.org/10. 1073/pnas.94.23.12366, PMID: 9356455

Ragona L, Pagano K, Tomaselli S, Favretto F, Ceccon A, Zanzoni S, D'Onofrio M, Assfalg M, Molinari H. 2014. The role of dynamics in modulating ligand exchange in intracellular lipid binding proteins. BBA-Proteins Proteom 1844:1268-1278. DOI: 10.1016/j.bbapap.2014.04.011, PMID: 24768771

Silvaroli JA, Arne JM, Chelstowska S, Kiser PD, Banerjee S, Golczak M. 2016. Ligand binding induces conformational changes in human cellular retinol-binding protein 1 (CRBP1) revealed by atomic resolution crystal structures. J Biol Chem 291:8528-8540. DOI: 10.1074/jbc.M116.714535, PMID:

26900151

Slater PG, Cerda CA, Pereira LA, Andres ME, Gysling K. 2016. CRF binding protein facilitates the presence of CRF type 2α receptor on the cell surface. Proc Natl Acad Sci USA 113:4075-4080. DOI: 10.1073/pnas.1523745113, PMID: 27035969

Smathers RL, Petersen DR. 2011. The human fatty acid-binding protein family: evolutionary divergences and functions. Hum Genomics 5:170-191. DOI: 10.1186/1479-7364-5-3-170, PMID: 21504868

Storch J, Thumser AE. 2010. Tissue-specific functions in the fatty acid-binding protein family. J Biol Chem 285:32679-32683. DOI: 10.1074/jbc.R110.135210, PMID: 20716527

Stremmel W, Pohl L, Ring A, Herrmann T. 2001. A new concept of cellular uptake and intracellular trafficking of long-chain fatty acids. Lipids 36:981-989. DOI: https://doi.org/10.1007/s11745-001-0809-2, PMID: 11724471

Tan NS, Shaw NS, Vinckenbosch N, Liu P, Yasmin R, Desvergne B, Wahli W, Noy N. 2002. Selective cooperation between fatty acid binding proteins and peroxisome proliferator-activated receptors in regulating transcription. Mol Cell Biol 22:5114-5127. DOI: 10.1128/MCB.22.14.5114- 5127.2002, PMID: 12077340

Thumser AE, Storch J. 2000. Liver and intestinal fatty acid-binding proteins obtain fatty acids from phospholipid membranes by different mechanisms. J Lipid Res 41:647-656. PMID: 10744786

Tochtrop GP, Richter K, Tang CG, Toner JJ, Covey DF, Cistola DP. 2002. Energetics by NMR: site-specific binding in a positively cooperative system. Proc Natl Acad Sci USA 99:1847-1852. DOI: 10.1073/pnas.012379199, PMID: 11854486

Tsfadia Y, Friedman R, Kadmon J, Selzer A, Nachliel E, Gutman M. 2007. Molecular dynamics simulations of palmitate entry into the hydrophobic pocket of the fatty acid binding protein. FEBS lett 581:1243-1247. DOI: 10.1016/j.febslet.2007.02.033, PMID: 17343854

Tsukamoto S, Fujiwara K, Ikeguchi M. 2009. Fatty acids bound to recombinant tear lipocalin and their role in structural stabilization. J Biochem 146:343-350. DOI: 10.1093/jb/mvp076, PMID: 19470520

Velkov T, Chuang S, Prankerd R, Sakellaris H, Porter CJ, Scanlon MJ. 2005. An improved method for the purification of rat liver-type fatty acid binding protein from Escherichia coli. Protein Expr Purif 44:23-31. DOI: 10.1016/j.pep.2005.04.006, PMID: 15914028

Weisiger RA. 2002. Cytosolic fatty acid binding proteins catalyze two distinct steps in intracellular transport of their ligands. Mol Cell Biochem 239:35-43. DOI: 10.1023/A:1020550405578, PMID: 12479566

Winn MD, Ballard CC, Cowtan KD, Dodson EJ, Emsley P, Evans PR, Keegan RM, Krissinel EB, Leslie AG, McCoy A, McNicholas SJ, Murshudov GN, Pannu NS, Potterton EA, Powell HR, Read RJ, Vagin A, Wilson KS. 2011. Overview of the CCP4 suite and current developments. Acta Crystallogr D Biol Crystallogr 67:235-242. DOI: 10.1107/S0907444910045749, PMID: 21460441

Xiao T, Fan JS, Zhou H, Lin Q, Yang D. 2016. Local unfolding of fatty acid binding protein to allow ligand entry for binding. Angew Chem Int Ed Engl 55:6869-6872. DOI: 10.1002/anie.201601326, PMID: 27105780

Yu BH, Yang DW. 2016. Coexistence of multiple minor states of fatty acid binding protein and their functional relevance. Sci Rep-UK 6. DOI: 10.1038/Srep34171, PMID: 27677899

Zamarreño F, Herrera FE, Córsico B, Costabel MD. 2012. Similar structures but different mechanisms: prediction of FABPs-membrane interaction by electrostatic calculation. Biochim Biophys Acta 1818:1691-1697. DOI: 10.1016/j.bbamem.2012.03.003, PMID: 22446190

Zhang J, Liu ZP, Jones TA, Gierasch LM, Sambrook JF. 1992. Mutating the charged residues in the binding pocket of cellular retinoic acid-binding protein simultaneously reduces its binding affinity to retinoic acid and increases its thermostability. Proteins 13:87-99. DOI: 10.1002/prot.340130202, PMID: 1377826

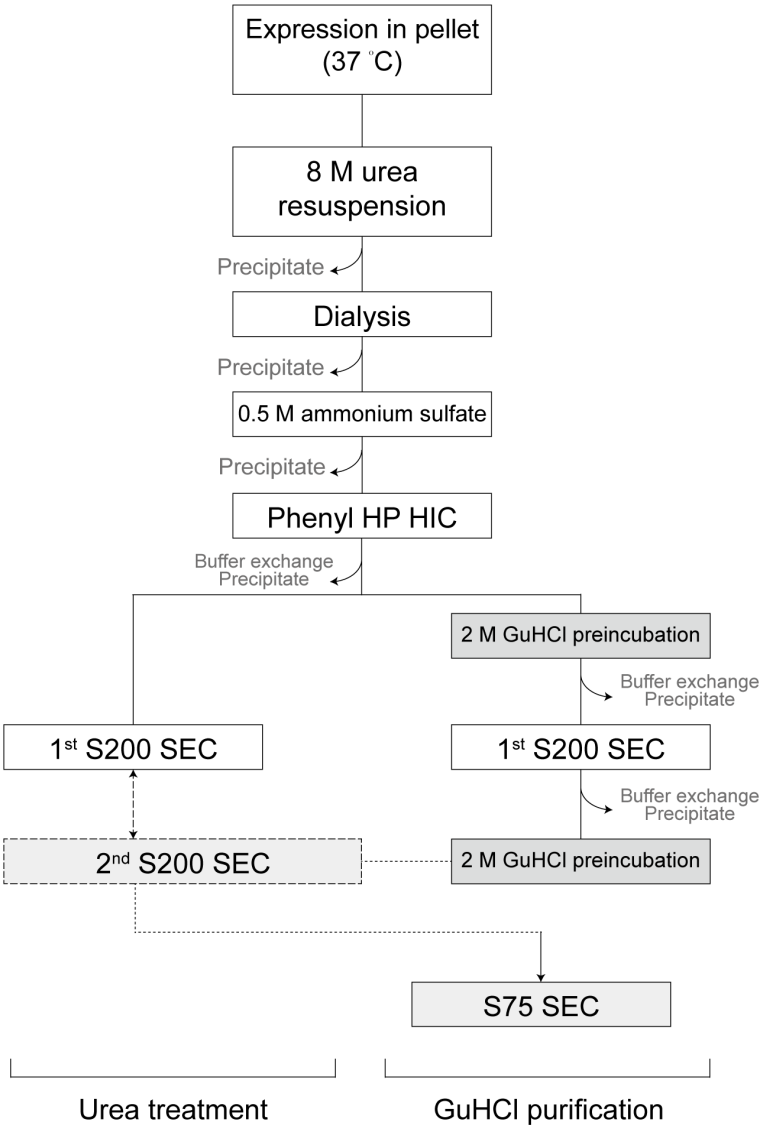

Supplementary Fig. S1. Scheme of the purification procedures for urea-treated and GuHCl-purified dFABP

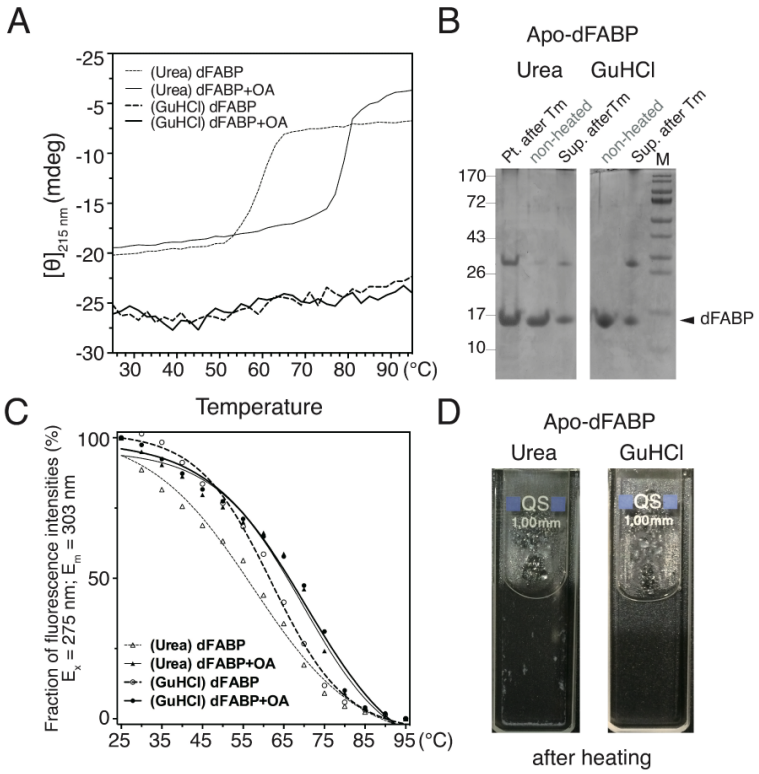

Supplementary Fig. S2. Comparison of thermal stability and sample solution after heating **(A)** CD thermal melting curves of urea-treated and GuHCl-purified samples were compared in the presence or absence of ligand OA. No apparent secondary conformational change was detected at 215 nm for the GuHCl-purified dFABP with or without the ligand OA. **(B)** SDS-PAGE analyses of the urea-treated and GuHCl-purified samples before and after heating in CD Tm experiments. The urea-treated sample showed solid precipitates after heating, whereas the GuHCl-purified sample showed a clear solution, with both supernatants displaying bands at higher molecular weights. **(C)** The unfolding curves derived from the intrinsic fluorescence spectra of urea-treated and GuHCl-purified dFABP in the presence or absence of the ligand OA were measured to determine the tertiary thermal stability. **(D)** The sample solution of GuHCl-purified apo-dFABP remained transparent after heating, whereas that of urea-treated apo-dFABP formed white solid precipitates.

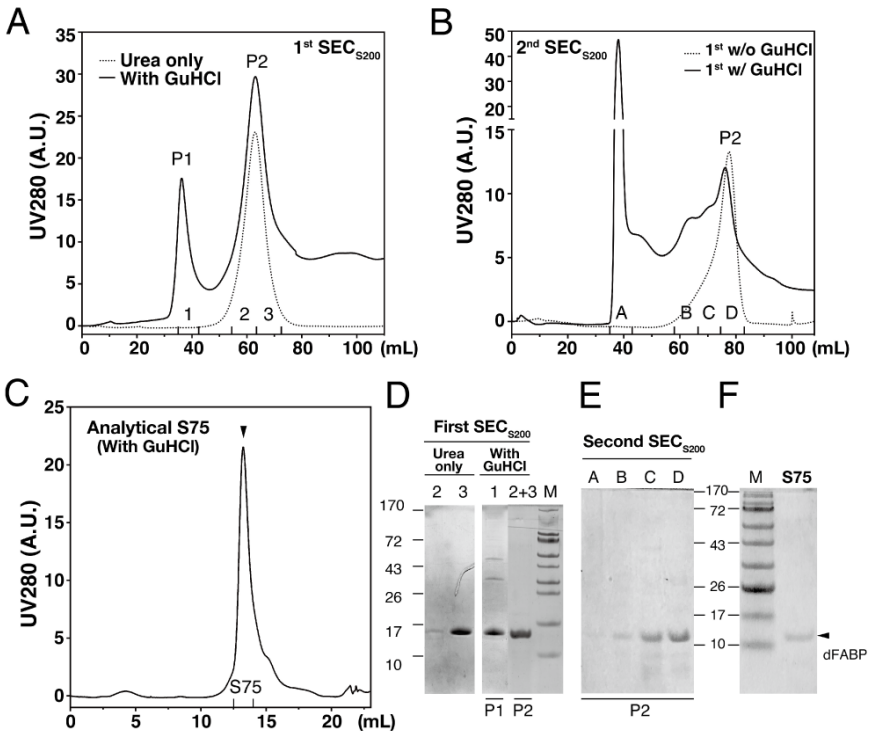

Supplementary Fig. S3. Comparison of the purification profiles of urea-treated and GuHCl-purified dFABP

(A) The first round of S200 size-exclusion chromatography (SEC) for HIC eluted samples is presented with (solid line) and without (dotted line) the 2 M GuHCl treatment. With the treatment, two groups of components were separated and denoted eluent P1 (1) and eluent P2 (2 and 3). **(B)** Eluent P2 of the GuHCl-purified dFABP from the first S200 SEC in the presence (solid-line) or absence (dotted line) of repeated 2 M GuHCl treatment is compared for the second round of S200 SEC. This step resulted in the separation of four components, denoted as eluents A, B, C and D. **(C)** Eluent D was finally confirmed by analytical S75 chromatography to be a single elution peak. The sample was preincubated with 2 M GuHCl before injection. **(D)** Eluents of the first round of S200 SEC from urea-treated and GuHCl-purified samples were analysed using SDS-PAGE and denoted as 1 (P1), 2 and 3 (P2). **(E)** SDS-PAGE analysis of the eluents in the second round of S200 SEC involving GuHCl-purified samples. Four isolated eluents (denoted A, B, C and D) were separated by repeated preincubation with 2 M GuHCl before the injection. **(F)** SDS-PAGE determination of the final fraction of S75 chromatography from the GuHCl-purified sample. The arrow indicates protein bands corresponding to the representative escort protein dFABP.

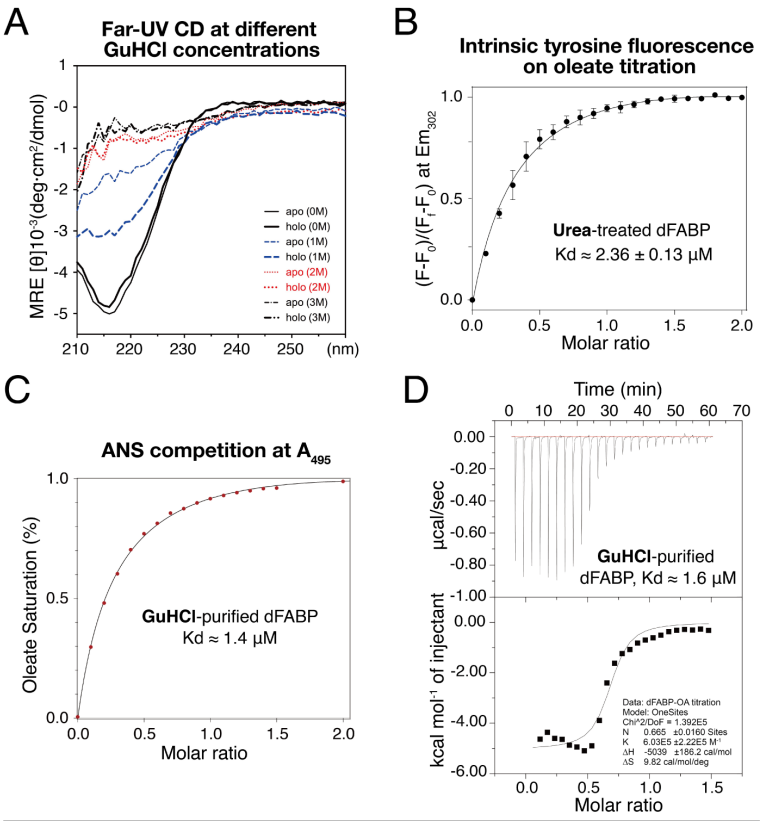

Supplementary Fig. S4. Biochemical properties of dFABP

(A) Urea-treated dFABP was titrated with GuHCl (0 M to 3 M) and monitored by far-UV CD. Both apo- and holo-dFABP were unfolded in 2 M GuHCl, and this concentration was used in the GuHCl purification. **(B)** OA binding assay based on the intrinsic fluorescence of urea-treated dFABP (5GGE): 6 μM protein was mixed with OA at a final molar ratio of 1:2. Data were collected using an excitation wavelength of 280 nm and an emission wavelength of 302 nm. The Kd was calculated to be approximately 2.4 μM. **(C)** ANS competition assay; 1 μM GuHCl-purified dFABP (5GKB) presaturated with 5 μM ANS was mixed with protein in competition with the ligand OA at a final molar ratio of 1:2, and ANS fluorescence (detected at 495 nm) was measured to enable the calculation of Kd calculation (approximately 1.4 μM). **(D)** GuHCl-purified dFABP at a concentration of 170 μM was subjected to iTC200 and titrated with OA at 30°C. The derived Kd is approximately 1.6 μM.

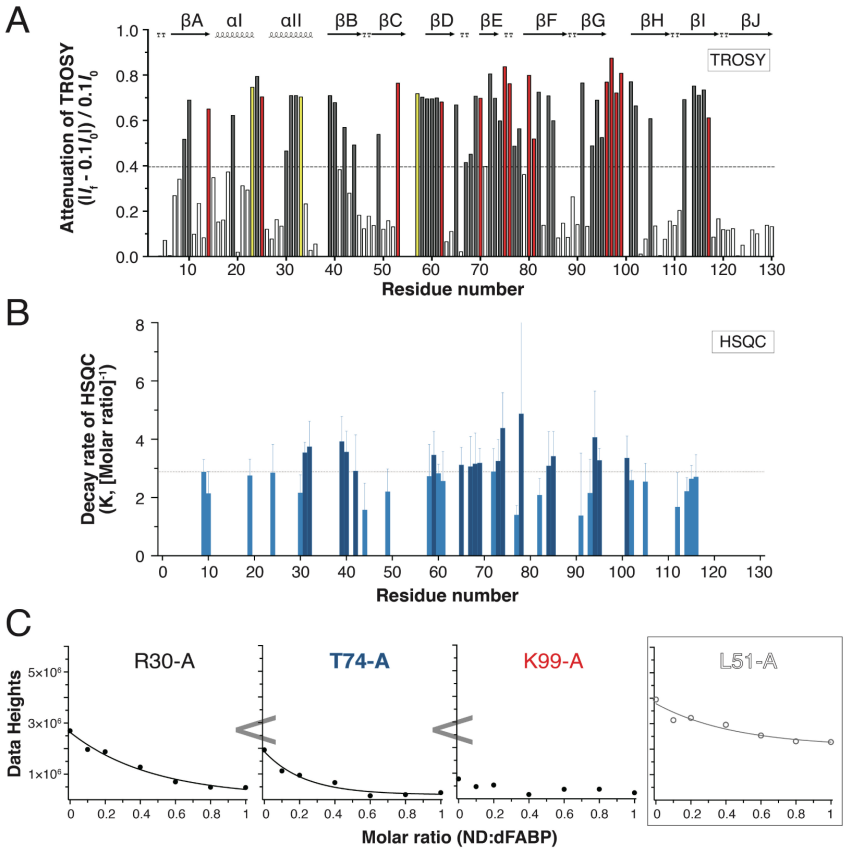

Supplementary Fig. S5. Membrane interaction pattern of apo-dFABP
(A) The fraction of attenuation was derived from TROSY spectra of 5GKB in the presence or absence of lipid ND (***Fig. 4C***). The average change is indicated by the dotted line. Residues labelled in red are decayed immediately; others above the average value were analysed further by lipid ND titration using a series of HSQC spectra. Residues shown in yellow are not assigned. **(B)** Residues with attenuation fractions above the average in the TROSY spectra were selected, and their decay rates were analysed using lipid ND HSQC titration. The signals of selected residues were fit to the one-phase decay model in GraphPad, and those above the average K (2.88 M^{-1}) were defined as faster decaying residues. **(C)** The residues were classified according to a combination of the attenuation fraction and signal decay rate, and representative residues appended with A indicate conformer-A. Residues with consistent intensities bracketed as L51-A are depicted in a thin sausage representation, as shown in ***Fig. 4D***. A single-exponential decay function was applied to all TROSY-selected residues, and three representative residues, namely, R30, T74 and K99, are plotted and coloured according to their decay patterns.

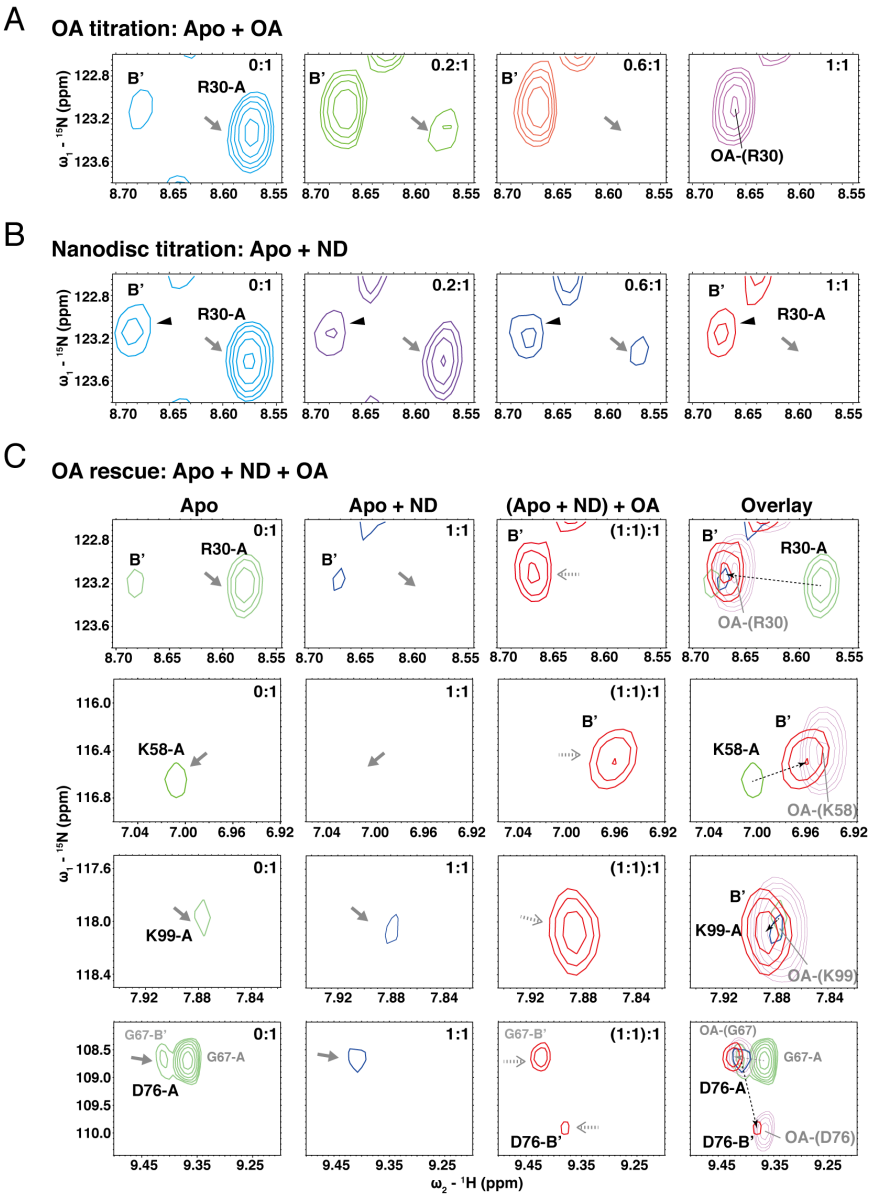

Supplementary Fig. S6. Comparisons of ligand binding and membrane interaction as analysed in the signal recovery study

(A) Four representative ratios in the ligand titration illustrated by R30. The grey arrow indicates the disappearance of conformer-A upon ligand titration, and in the final spectrum, the OA-liganded cross-peak in labelled with the representative residue in brackets. **(B)** Four representative ratios in the lipid ND titration are illustrated by R30. The signal for conformer-B' of R30 in apo-dFABP changes very little (black arrow), whereas the signal for conformer-A continues to broaden (grey arrow). **(C)** Four representative residues with higher levels of disappearance, as seen in ***Fig. 4D***, in an OA rescue experiment. The signals of conformer-A (grey arrow) of apo-dFABP that disappeared after interaction with membrane mimetics are recovered as conformer-B' (grey dotted arrow) after the addition of ligand OA. The final comparison panel plots the preceding spectra together with the OA-liganded spectrum (light magenta), and a dotted arrow links the initial (green) and the rescued (red) signals.

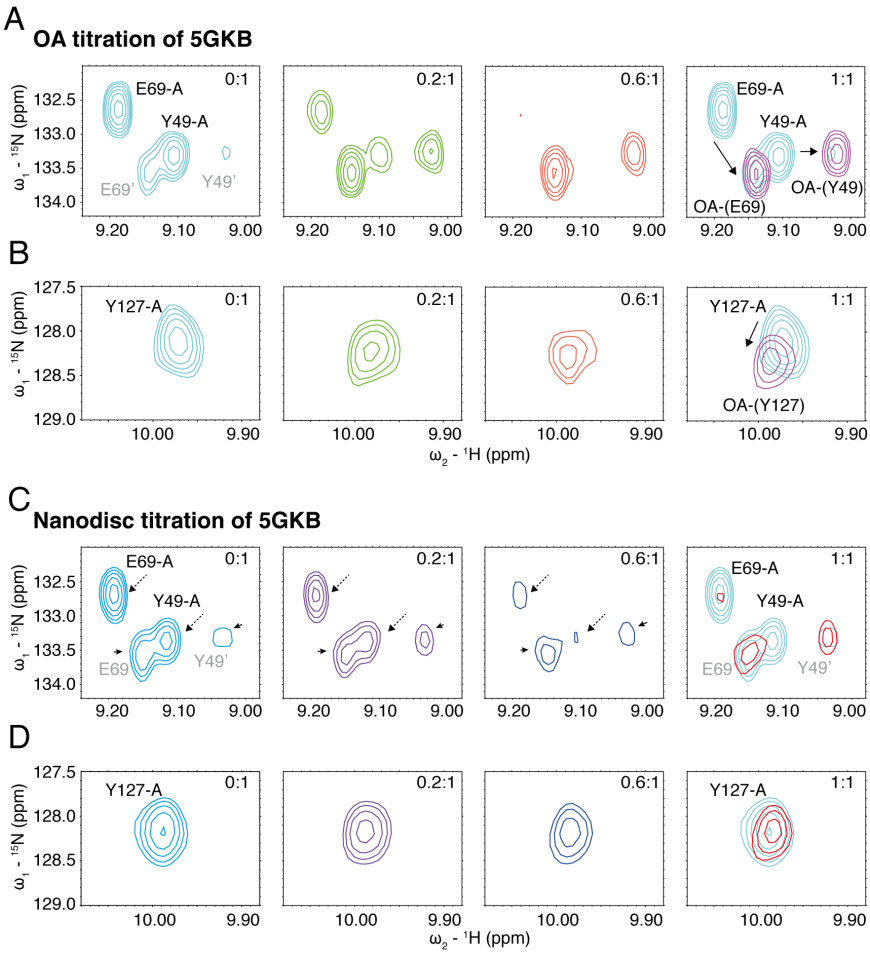

Supplementary Fig. S7. Comparison of residues in different regions of dFABP in terms of their effects on ligand binding and membrane interaction

(A, B) Four representative ratios used in the ligand titration of GuHCl-purified apo-dFABP are presented. The ligand OA titration for E69 and Y49, which are located near the membrane attachment (βE) and ligand entry (βB) sites, respectively, shows that conformer-A disappeared sooner during ligand binding. The ligand titration of Y127, which controls binding to the carboxylate heads of ligands, indicates that CSP occurred upon ligand binding (the arrow indicates CSP). **(C, D)** Four representative ratios used in the lipid ND titration of GuHCl-purified apo-dFABP are presented. The lipid ND titrations for E69 and Y49 show that conformer-A disappeared more slowly during lipid ND titration (dashed arrows) than during ligand titration. In contrast, the conformer-B' of both residues was nearly unchanged (arrows) during membrane attachment. The lipid ND titration of Y127 indicates few CSP changes upon lipid interaction.

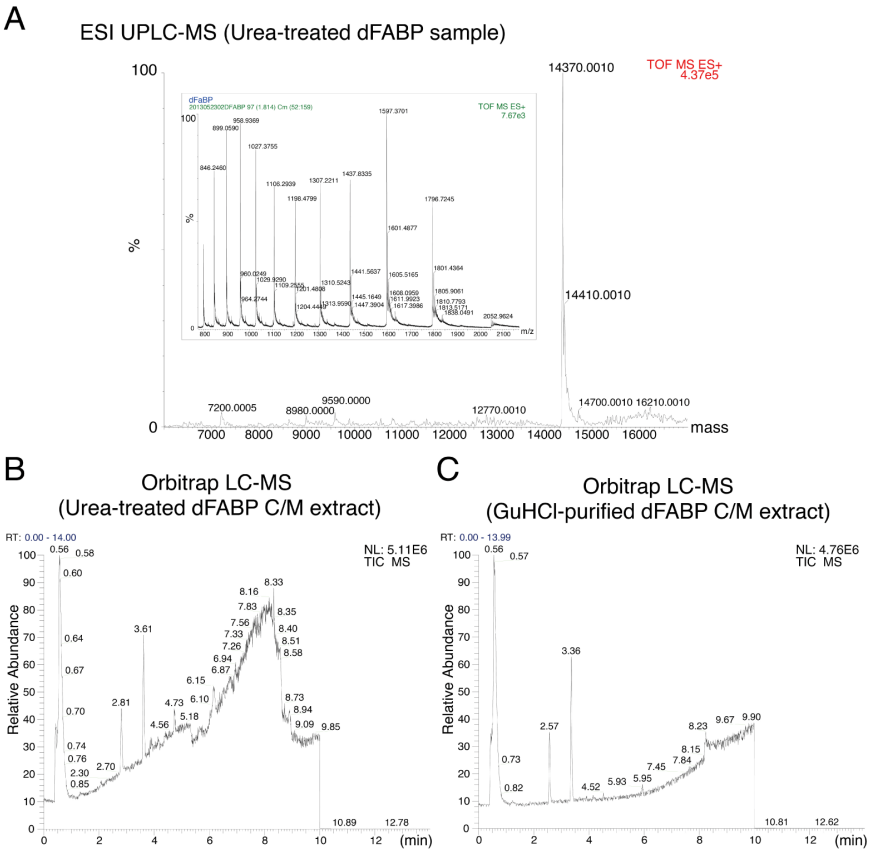

Supplementary Fig. S8. Mass spectrometry of urea and GuHCl-purified dFABP
(A) The theoretical molecular weight of dFABP is 14,371 Da. The urea-treated dFABP was analysed by ESI Q-TOF UPLC-MS (Bruker, MA, USA). **(B, C)** Samples from urea and GuHCl purifications were quantified using the Bradford protein assay. Each protein solution containing 6.8 μg dFABP was taken as sample for chloroform/methanol (1:1) extraction. The preceding hydrophobic compound extracts were subjected to Thermo LTQ Orbitrap liquid chromatography–mass spectrometry analysis with an ACQUITY UPLC HSS T3 column (Waters, USA)

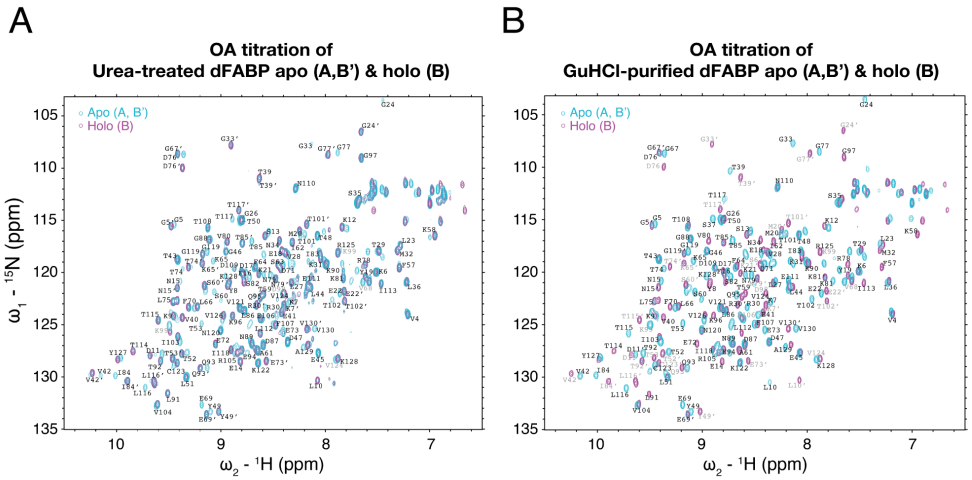

Supplementary Fig. S9. Comparison of NMR HSQC spectra in the presence and absence of ligand OA in samples with different conformational homogeneity

(A) The final holo form (magenta) is superimposed with the initial apo form (cyan) to compare the cross-peak dispersion of OA titration in urea-treated dFABP through HSQC. **(B)** The final holo form (magenta) is superimposed with the initial apo form (cyan) to compare the cross-peak dispersion of OA titration in GuHCl-purified dFABP through HSQC. Residues labelled with a symbol prime represent conformer-B', and residues coloured in grey exhibit a relatively low proportion compared to conformer-A.

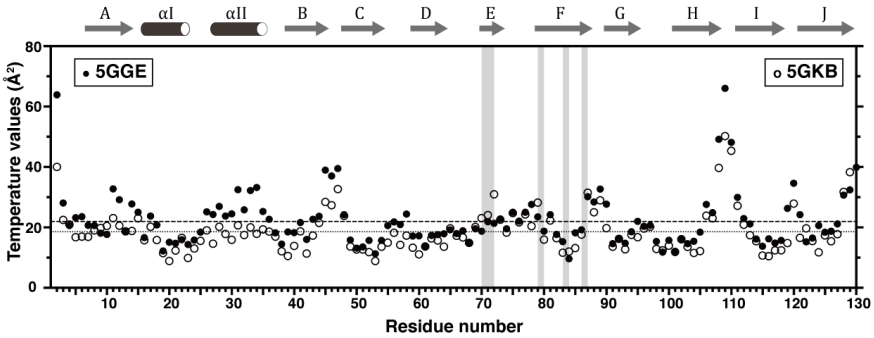

Supplementary Fig. S10. Temperature values of dFABP crystal structures
Each Cα was plotted as a solid circle (5GGE) and an empty circle (5GKB) with the y-axis on the left and right. Higher values of residues in the gap region (βE and βF) of 5GKB are highlighted in grey stripes. Dashed and dotted lines are the average values of 5GGE and 5GKB, respectively.

Residue	P(H-N)	^{1}HN	^{15}N	^{13}CO	^{13}C$^{\alpha}$	^{13}C$^{\beta}$	Residue	P(H-N)	^{1}HN	^{15}N	^{13}CO	^{13}C$^{\alpha}$	^{13}C$^{\beta}$
MET^{1}	0						LEU^{66}	1	9.238	123.25	179.82	55.8	40.4
SER^{2}	0			172.96	55.7		GLY^{67}	1	9.428	108.6	173.42	46.3	
PHE^{3}	0.483	7.896	128.22	175.58	57.1	39.8	VAL^{68}	0.005					
VAL^{4}	1	7.184	124.03	177.8	64.2	31.1	GLU^{69}	1	9.152	133.56	175.29	57.3	31.1
GLY^{5}	1	9.5	115.56	174.26	45.5		PHE^{70}	1	9.319	123.3	172.79	55.5	
LYS^{6}	1	7.534	119.92	174.81		33.9	ASP^{71}	1	8.446	119.62	174.97	54.4	41.9
LYS^{7}	1	8.416	123.11	175.55	55.7	34.6	GLU^{72}	1	9.066	126.84	174.28	55.1	
TYR^{8}	1	8.946	121.23	174.69	56.6	42	GLU^{73}	1	8.58	128.41	177.82	54.2	30.1
LYS^{9}	1	9.466	124.19	176.88	54.9	36.6	THR^{74}	1	9.324	119.45	178.24	62	70.7
LEU^{10}	1	8.096	130.36	174.28	57.8	42.1	LEU^{75}	1	9.435	122.69	177.44	58.4	43.6
ASP^{11}	1	9.69	127.96		55.1		ASP^{76}	1	9.379	110	175.41	53.1	39.7
LYS^{12}	1	7.853	115.61	174.27	55.3	36.2	GLY^{77}	1	7.988	108.7	175.5	45.8	
SER^{13}	1	8.594	116.48	173.42	57	64.4	ARG^{78}	1	7.631	119.23	175.57	55.8	31.6
GLU^{14}	1	8.824	128.5	176.08	55.3	32.7	ASN^{79}	1	8.497	120.65	175.12	53.5	39.8
ASN^{15}	1	9.432	121.5			38.3	VAL^{80}	1	8.951	117.05	174.9	58.4	35.7
PHE^{16}	1	8.801	120.19	177.88	59.1	39	LYS^{81}	1	7.846	120.53		54.3	33.8
ASP^{17}	1	8.815	119.97	178.31	58.9	41.9	SER^{82}	1	8.792	120.94	172.16	56.7	67.6
GLU^{18}	1	8.417	117.92	179.06	60.1	28.6	ILE^{83}	1	8.064	118.22	174.23	61.5	42
TYR^{19}	1	7.624	120.28	175.79	62.7	38.9	ILE^{84}	1	9.904	130.4	175.15	59.9	38.7
MET^{20}	1	8.261	115.97	178.71		34.4	THR^{85}	1	8.81	117.18	172.41	59.7	72.2
LYS^{21}	1	8.649	120.11	180.82	60.3	32.2	LEU^{86}	1	8.785	123.61	175.04	54	47.6
GLU^{22}	1	7.836	121.8	178.13	58.3	29	ASP^{87}	1	8.607	127	176.83	53.1	42.7
LEU^{23}	1	7.296	117.39	177.3	55.3	43.6	GLY^{88}	1	9.129	116.81	173.61	47.9	
GLY^{24}	1	7.673	106.58	174.88	45		ASN^{89}	1	8.729	126.85	173.41	52.5	38.4
VAL^{25}	0.004						LYS^{90}	1	8.006	119.22	175.63	55.3	34.2
GLY^{26}	0			174.46	45.3		LEU^{91}	1	9.528	131.67	177.44	53.2	45.4
LEU^{27}	1	8.332	121	178.89	59.4	42.4	THR^{92}	1	9.589	128.51	171.44	64.3	69.4
VAL^{28}	1	8.392	118.12	178.65	66.8	31.3	GLN^{93}	1	9.207	129.12	173.69	53.4	30.6
THR^{29}	1	7.511	117.93	176.47	999	67.5	GLU^{94}	1	8.811	127.39	176.09	999	31.1
ARG^{30}	1	8.672	123.07	178.4	59.8	30.1	GLN^{95}	1	8.637	122.38	176.39	54.7	30.2
LYS^{31}	1	8.062	118.69	180.62	59.8	31.8	LYS^{96}	1	8.903	124.15		55.6	32.9
MET^{32}	1	7.328	117.88	179.26	57.7		GLY^{97}	1	7.666	109.05	173.34	44.7	
GLY^{33}	1	8.921	107.81	175.52	48		ASP^{98}	0.006					
ASN^{34}	1	8.458	116.95	175.91	55.2	39.5	LYS^{99}	0.009					
SER^{35}	1	7.688	113.04	174.57	59.2	65	PRO^{100}	0			176.39	63.2	32.2
LEU^{36}	1	7.233	120.84		54.9	44.3	THR^{101}	1	8.196	115.34	171.05	59.5	70.6
SER^{37}	0						THR^{102}	1	7.83	122.73	173.35	61.7	71.1
PRO^{38}	0			175.25	62.3	34.2	ILE^{103}	1	9.423	126.16	176.16	61.1	41.1
THR^{39}	1	8.648	111.04	174.14	60.4	71.6	VAL^{104}	1	9.616	132.61	174.28	62.2	33.6
VAL^{40}	1	9.387	124.32		61.2	36	ARG^{105}	1	8.856	127.68	173.01	54.8	32.5
GLU^{41}	1	8.437	123.82	175.07	55.5	35.3	GLU^{106}	1	8.635	124.46	174.97	54.7	31.7
VAL^{42}	1	10.288	129.77	175.45	60.8	33.3	PHE^{107}	1	8.493	124.97	176.88	58.5	41.8
THR^{43}	1	9.431	118.68	172.32	60.1	71.6	THR^{108}	1	9.154	115.43	174.88	60.2	71.9
LEU^{44}	1	8.161	121.39	174.77	54.5	46.2	ASP^{109}	1	8.889	119.54	176.62	57.7	40.3
GLU^{45}	1	8.083	127.64	176.25	55.1	31.2	ASN^{110}	1	8.292	111.8	175.66	53.7	40.8
GLY^{46}	1	8.968	117.96	173.4	47.6		GLU^{111}	1	8.184	121.41	172.05	55.7	34.4
ASP^{47}	1	8.377	126.68	175.17	52.9	41.1	LEU^{112}	1	8.643	125.81	179.73	52.8	43.4
THR^{48}	1	8.093	116.46	174.6	62.5	69.9	ILE^{113}	0.928	7.479	121.06	179.86	60.6	39.1
TYR^{49}	1	9.034	133.31	176.99	57.6	42	THR^{114}	1	9.855	127.53	172.91	61.4	70.5
THR^{50}	1	8.815	114.98	173.07	61.8	71.6	THR^{115}	1	9.612	124.57	174.56	61.7	69.5
LEU^{51}	1	9.35	129.98	176.52	54.5	45.3	LEU^{116}	1	9.652	130.4	175.62	54.8	42.8
THR^{52}	1	9.392	127.74	174.31	62.7	69.7	THR^{117}	1	8.841	114.04	175.89	60.2	71.5
THR^{53}	1	9.473	128.16	179.26	62	999	ILE^{118}	1	8.914	127.38	174.15	60.6	40.4
THR^{54}	0						GLY^{119}	1	9.19	118.27	175.42	47.3	
SER^{55}	0						ASN^{120}	1	9.017	125.6	175.12	52.9	38.6
THR^{56}	0			175.02	64.4	68.5	VAL^{121}	1	8.83	123.38	174.37	63.4	32.5
PHE^{57}	1	7.309	119.54	174.64	58.3	41.8	LYS^{122}	1	8.661	128.65	174.84	54.8	35.1
LYS^{58}	1	6.965	116.43	174.81	56.3	36.7	CYS^{123}	1	9.431	128.66	172.96	55.7	28.8
THR^{59}	1	8.602	121.99	173.87	61.7	71.3	VAL^{124}	1	8.415	121.98	177.01	57.0	
SER^{60}	1	9.171	121.22	172.2	56.5	65.8	ARG^{125}	1	7.896	118.06	173.88	54.6	34.9
ALA^{61}	1	8.66	127.49	177	51.3	21.9	VAL^{126}	1	8.986	124.09	175.55	61.8	34
ILE^{62}	1	8.335	117.09	174.7	59.4	41.6	TYR^{127}	1	10.002	128.25		55.8	
SER^{63}	1	8.472	119.27	173.23	57.2	65.3	LYS^{128}	0.486	7.896	128.22	176.54	54.6	35.4
PHE^{64}	1	8.684	119.41	172.66	55.7	40.4	ALA^{129}	1	8.161	126.91		53	18.7
LYS^{65}	1	9.19	119.14	178.03	54.2	34.4	VAL^{130}	1	8.198	125.39		63.5	33.3

Supplementary Table S11. Sequential chemical shift assignments of ^{15}N/^{13}C OA-dFABP (BMRB ID: 27112)

Autoassignment was assisted with MANI PINE server v.2.0. The MANI PINE reports were manually inspected through Sparky and subsequently removed, as summarized here. The assignments of ^{1}H, ^{15}N, and ^{13}C chemical shifts were deposited into the BioMagResBank database under the accession number 27112.

Residue	P(H-N)	^{1}HN	^{15}N	^{13}CO	^{13}C$^{\alpha}$	^{13}C$^{\beta}$	Residue	P(H-N)	^{1}HN	^{15}N	^{13}CO	^{13}C$^{\alpha}$	^{13}C$^{\beta}$
MET^{1}	0						LEU^{66}	1	9.169	123.13	169.21	53.2	
SER^{2}	0.987	7.629	113.18	174.28	56.6	62.6	GLY^{67}	1	9.289	108.50	175.53	43.6	
PHE^{3}	0.948	8.371	119.08	173.45	54.3	37.3	VAL^{68}	1	7.562	120.74	172.18	59.1	
VAL^{4}	1	7.109	123.76	171.13	61.4	28.6	GLU^{69}	0.998	9.102	132.58	174.04		
GLY^{5}	1	9.396	115.33	174.71	42.9		PHE^{70}	0.716	8.974	126.71	172.00	60.2	39.3
LYS^{6}	1	7.437	119.74	174.11	52.7	31.4	ASP^{71}	0.998	8.728	114.74	174.54		
LYS^{7}	1	8.275	122.65	171.09	56.4	36.4	GLU^{72}	0.997	8.246	120.76	174.05	56.7	
TYR^{8}	0.525	8.730	119.79				GLU^{73}	0.697	7.386	120.78		60.2	29.4
LYS^{9}	0						THR^{74}	0.694	8.119	115.28			
LEU^{10}	0.534	8.552	125.62	174.68	55.2	39.3	LEU^{75}	0.377	9.000	118.75	171.58	55.7	
ASP^{11}	1	9.578	127.66	173.97	52.5	43.5	ASP^{76}	1	9.333	109.25	173.62	50.5	
LYS^{12}	1	7.742	115.53	174.64	52.6	33.5	GLY^{77}	1	7.812	108.34	173.41	43.3	
SER^{13}	1	8.476	116.08	175.53	54.4	61.7	ARG^{78}	1	7.537	119.08	173.39	55.2	29.0
GLU^{14}	1	8.754	128.24	172.87	52.6	30.1	ASN^{79}	1	8.398	120.37	173.82	50.8	37.2
ASN^{15}	1	9.357	121.37	172.89	51.6		VAL^{80}	1	8.885	117.01			
PHE^{16}	0.995	8.652	120.31	171.20	57.0		LYS^{81}	0.337	8.264	115.87	173.67	59.6	31.5
ASP^{17}	0.917	8.682	119.82		56.1		SER^{82}	1	8.560	111.31	172.02	57.8	
GLU^{18}	0						ILE^{83}	1	9.766	127.08	174.98	58.5	
TYR^{19}	1	7.534	120.13		60.0	36.3	ILE^{84}	1	9.928	129.73	173.81	57.3	36.0
MET^{20}	1	8.163	115.72	170.32	57.5	31.8	THR^{85}	1	8.729	117.00	176.57	57.0	69.5
LYS^{21}	1	8.556	119.93	168.5	57.5	29.6	LEU^{86}	1	8.697	123.47	173.88	51.3	44.9
GLU^{22}	1	7.786	121.75	170.82	55.6	26.4	ASP^{87}	1	8.523	126.75	172.16	50.5	40.0
LEU^{23}	1	7.222	117.23	171.70	52.7	41.2	GLY^{88}	1	9.037	116.64	175.30	45.3	
GLY^{24}	1	7.568	106.16		42.2		ASN^{89}	1	8.637	126.62	175.54	49.8	35.8
VAL^{25}	0.243	8.040	107.64				LYS^{90}	1	7.922	118.99	173.32	52.5	31.5
GLY^{26}	0.367	8.044	107.60	171.99	48.5		LEU^{91}	1	9.438	131.36	172.51	51.9	42.8
LEU^{27}	0.996	8.252	116.89	170.03	56.7	39.7	THR^{92}	1	9.252	127.43	174.65	59.9	67.0
VAL^{28}	1	8.300	117.98	170.27	64.0	28.7	GLN^{93}	1	9.387	127.89		57.0	27.5
THR^{29}	1	7.435	117.82		63.8		GLU^{94}	0.998	7.959	118.67		58.0	
ARG^{30}	0.111	7.752	122.68	173.88	59.0		GLN^{95}	1	9.365	124.19	172.58	52.1	27.8
LYS^{31}	0.999	8.639	116.79	168.38	57.0		LYS^{96}	1	8.832	124.04	173.10	52.8	30.3
MET^{32}	1	7.256	117.67	169.59	55.0		GLY^{97}	1	7.569	109.98	175.60	40.0	
GLY^{33}	1	8.942	107.84	173.32	45.2		ASP^{98}	1	8.339	121.93	171.93	54.3	38.0
ASN^{34}	1	8.371	117.23	173.10	52.6	36.8	LYS^{99}	1	7.786	117.76		50.0	30.6
SER^{35}	1	7.590	112.91	174.44	56.4	62.3	PRO^{100}	0			172.59	60.5	
LEU^{36}	1	7.153	120.80	172.08	52.3	41.6	THR^{101}	0.296	8.111	115.25	177.92		
SER^{37}	0						THR^{102}	0.613	7.83	122.73	173.35	61.7	71.1
PRO^{38}	0			177.48	61.5		ILE^{103}	1	9.338	126.08	172.77	58.3	38.5
THR^{39}	1	7.513	117.86	172.23	63.5		VAL^{104}	1	9.537	132.46	173.13	59.6	31.0
VAL^{40}	1	8.498	123.13		58.2		ARG^{105}	0.208	8.540	124.29	174.00	52.0	29.1
GLU^{41}	0.987	8.395	123.95	173.80	52.8		GLU^{106}	1	8.635	124.46	174.97	54.7	31.7
VAL^{42}	1	10.093	129.76	173.51	58.0	30.7	PHE^{107}	1	8.409	124.77	172.08	55.7	39.2
THR^{43}	1	9.343	118.57	176.62	57.3	68.9	THR^{108}	1	9.059	115.38	174.03	57.5	69.1
LEU^{44}	1	8.063	121.27	174.19			ASP^{109}	1	8.805	119.39	172.34	55.0	37.6
GLU^{45}	1	7.993	127.54	172.69	52.3	28.6	ASN^{110}	1	8.206	111.67	173.72	50.8	38.2
GLY^{46}	1	8.878	117.79	175.55	44.9		GLU^{111}	0.529	9.003	118.75	173.68	54.5	28.4
ASP^{47}	1	8.377	126.68	175.17	52.9	41.1	LEU^{112}	0.996	9.225	123.22	176.20		
THR^{48}	1	7.974	116.11	174.33	59.8	67.2	ILE^{113}	0.682	8.338	119.23	177.28	56.8	
TYR^{49}	1	9.019	133.10		54.9		THR^{114}	0.623	7.874	122.38	176.09	58.6	67.8
THR^{50}	0						THR^{115}	0.656	9.525	124.40	174.42	59.0	66.8
LEU^{51}	0.627	8.887	120.25	176.17			LEU^{116}	0.971	9.595	130.19	173.39	52.0	40.1
THR^{52}	0.743	9.283	119.43	171.07			THR^{117}	1	8.778	113.83	173.48	57.4	68.8
THR^{53}	0.792	9.219	119.35			68.0	ILE^{118}	1	8.797	127.07	174.80	57.6	
THR^{54}	0.273	9.524	124.39	175.01	59.3	67.1	GLY^{119}	1	9.060	117.79	173.93	43.4	
SER^{55}	0.416	9.385	122.63		53.8	63.1	ASN^{120}	0.911	9.615	119.63	173.82	50.2	36.0
THR^{56}	0.658	8.576	127.40	173.88	61.6	65.7	VAL^{121}	1	8.748	123.24	174.58	60.7	29.9
PHE^{57}	1	7.220	119.06	174.21	55.5	39.0	LYS^{122}	1	8.570	128.45		52.2	32.4
LYS^{58}	1	6.924	116.38	174.16	53.6	33.8	CYS^{123}	1	9.367	128.63	176.00	53.0	26.1
THR^{59}	1	8.532	122.04		59.0	68.5	VAL^{124}	1	7.816	128.11	177.40	58.7	
SER^{60}	0.182	8.127	116.17	177.50	56.3	64.3	ARG^{125}	1	9.531	130.47			
ALA^{61}	1	9.077	128.98	175.31	50.7		VAL^{126}	1	8.908	124.26	174.17	59.0	
ILE^{62}	1	8.736	127.27	175.12	59.3		TYR^{127}	0.996	9.890	128.01	173.60		
SER^{63}	0.999	8.999	121.71	176.83	54.0	65.1	LYS^{128}	0.996	8.857	120.66	172.46	52.1	
PHE^{64}	0.998	7.977	118.04	174.68	58.7	39.3	ALA^{129}	1	8.126	126.97	171.52	50.4	16.1
LYS^{65}	0.900	9.833	130.26			31.8	VAL^{130}	1	8.038	125.17			

Supplementary Table S12. Sequential chemical shift assignments of ^{15}N/^{13}C apo-dFABP (BMRB ID: 27113)

The ^{1}H, ^{15}N, and ^{13}C chemical shifts of apo-dFABP were assigned through comparison to rule out the sequential assignments of liganded OA-dFABP and deposited in the BioMagResBank database under the accession number 27113.

Dataset	Monomer
Protein sample	dFABP$_{2\text{-}130}$ (5GGE)
Beamline	NSRRC_BL13B1
Wavelength (Å)	0.97622
Resolution (Å)	27.05-1.86 (1.93-1.86)
Space group	I422
Unit cell dimensions	
a, b, c (Å)	61.70, 61.70, 137.32
a, b, g (ɟ)	90
Unique reflections	11518
Total observations	79527
Redundancy	6.9 (6.2)
Completeness (%)	99.5
Mean I/S (I)	27.277 (3.2)
Solvent content (%)	41.6
R merge	0.068
Refinement	
Resolution range (Å)	27.052-1.861
No. of reflections	26.98-1.86 (1.93-1.86)
No. of protein atoms	2229
No. of water molecules	139
Average B-factors (Å^2)	30
R work/R free	0.179/0.246
Ramachandran plot statistics (%)	
Most favored regions	99.21
Additional allowed regions	0.85
Generously allowed regions	0.79
Disallowed regions	0.00
Rmsd bond length (Å)	0.56
Rmsd bond angle (˚)	0.69

Dataset	Monomer
Protein sample	dFABP$_{2\text{-}130}$ (5GKB)
Beamline	NSRRC_BL13C1
Wavelength (Å)	0.97622
Resolution (Å)	30.00-2.04 (2.11-2.04)
Space group	I422
Unit cell dimensions	
a, b, c (Å)	61.60, 61.60, 137.06
a, b, g (ɟ)	90
Unique reflections	8811
Total observations	81557
Redundancy	9.3 (9.1)
Completeness (%)	99.9
Mean I/S (I)	26.900 (6.1)
Solvent content (%)	45.1
R merge	0.100
Refinement	
Resolution range (Å)	28.091-2.039
No. of reflections	28.091-2.04 (2.11-2.04)
No. of protein atoms	2146
No. of water molecules	128
Average B-factors (Å^2)	24
R work/R free	0.186/0.241
Ramachandran plot statistics (%)	
Most favored regions	98.41
Additional allowed regions	2.59
Generously allowed regions	1.59
Disallowed regions	0.00
Rmsd bond length (Å)	0.77
Rmsd bond angle (˚)	0.83

Supplementary Table S13. Structure statistics of crystallographic data

	Apo	Apo + ND	Fraction of attenuation	Holo	Holo + ND	Fraction of attenuation
Residue	I_0	I_f	$\lvert I_f - 0.1I_f\rvert/0.1I_0$	I_0	I_f	$\lvert I_f - I_0\rvert/I_0$
V4	102059656	10236169	0.003	57453128	78385112	0.364
G5	47288044	4389232	0.072	41196720	45754608	0.111
K6	100498408	10004599	0.005	59593892	76520176	0.284
K7	51350968	3754745	0.269	47263984	47638508	0.008
Y8	37931528	2500352	0.341	29671190	41380316	0.395
K9	50540988	2442100	0.517	25914096	31046130	0.198
L10	13167488	408376	0.690	26716432	13971254	0.477
D11	30579616	2756910	0.098	22290676	27510230	0.234
K12	40389896	4986468	0.235	31912974	43327876	0.358
S13	44587316	4090012	0.083	41674232	44828176	0.076
E14	29433458	1028791	0.650	32607412	28197700	0.135
N15	41519752	2707878	0.348	33378808	42184864	0.264
F16	53035452	4496050	0.152	35610288	64646056	0.815
D17	53587956	4496050	0.161	42432080	64646056	0.524
E18	41125312	2578051	0.373	41762300	23567050	0.436
Y19	36330800	1371478	0.623	32587724	27299032	0.162
M20	29291386	2986628	0.020	36352260	34012964	0.064
K21	42373052	2913828	0.312	38084528	44066804	0.157
E22	30994032	4008471	0.293	38224716	39349064	0.029
L23	33140102	839221	0.747	38366136	17494090	0.544
G24	29911718	616473	0.794	29110736	13676654	0.530
V25	36547724	1081359	0.704	32051128	27120450	0.154
G26	119013384	10465228	0.121	86537120	98805128	0.142
L27	61610444	6636268	0.077	42993672	53271368	0.239
V28	87086464	7287488	0.163	50003608	64822052	0.296
T29	34693780	3003827	0.134	47456168	33107848	0.302
R30	38688728	2066465	0.466	39371616	37461168	0.049
K31	69153184	2006797	0.710	40640920	47087452	0.159
M32	30264064	878983	0.710	41387144	20751034	0.499
G33	15516145	460039	0.704	26655456	16086489	0.397
N34	16984862	1304392	0.232	33334536	31296824	0.061
S35	69028184	6711601	0.028	48834140	69159264	0.416
L36	54521812	5152728	0.055	47668664	55381036	0.162
T39	19079124	554021	0.710	34238664	15300431	0.553
V40	17693696	568693	0.679	34396800	16594798	0.518
E41	31688684	1954089	0.383	46951380	41617796	0.114
V42	25888518	1114666	0.569	24238218	25384872	0.047
T43	131238840	9450782	0.280	50211528	68131064	0.357
L44	58651200	2982944	0.491	54715776	68216064	0.247
E45	116395264	9519416	0.182	57113520	70489568	0.234
G46	78307696	6872092	0.122	39592288	48216744	0.218
D47	111539096	9165391	0.178	68461184	69591800	0.017
T48	131907480	11380362	0.137	65622736	80784752	0.231
Y49	37456908	1730016	0.538	36364664	29917378	0.177
T50	119013384	10465228	0.121	87602064	98805128	0.128
L51	87240472	7345301	0.158	42929596	53885616	0.255
T52	30508848	2651447	0.131	35977660	35235612	0.020
T53	36691204	863502	0.765	42559692	24199334	0.431
F57	22181638	624810	0.718	41251952	13049290	0.684
K58	33433942	994915	0.702	45554336	20605960	0.548
T59	50378792	1535512	0.695	44407964	33283802	0.250
S60	53569444	1630639	0.696	43041948	30692192	0.287
A61	74485616	2240313	0.699	63687116	58144560	0.087
I62	37089456	1181830	0.681	40665156	30377078	0.253
S63	48617392	4541397	0.066	38503808	52424112	0.362
F64	94833368	8430593	0.111	53578840	68016424	0.270
K65	38234856	1266239	0.669	31107304	20010692	0.357
L66	52828548	5393597	0.021	50284720	52472796	0.044
G67	44394024	2598262	0.415	35573708	35189952	0.011
V68	68566104	3765098	0.451	62578320	54556180	0.128
E69	54343868	1591521	0.707	42313528	35723884	0.156
F70	36069284	1088952	0.698	35614896	17473644	0.509
D71	62591720	3773711	0.397	36621320	52424112	0.432
E72	39360696	767073	0.805	40538684	18462140	0.545
E73	23224158	701332	0.698	38203740	14825069	0.612
T74	26391516	1060854	0.598	36210448	22756350	0.372
L75	13825667	225428	0.837	32764628	12339260	0.623
D76	22039212	524594	0.762	35148544	13759992	0.609
G77	34137036	1750490	0.487	34579872	31837884	0.079
R78	33101106	1444323	0.564	38606456	28467312	0.263
N79	49918880	3188134	0.361	39882056	40763016	0.022
V80	29951526	601823	0.799	38683736	13408120	0.653
K81	47073976	2266050	0.519	40590356	35672176	0.121
S82	19473498	536052	0.725	33815956	64646056	0.912
I83	73684320	6349858	0.138	39823588	55459520	0.393
I84	30014670	873856	0.709	32257152	18717910	0.420
T85	53439632	2142209	0.599	41053936	36458804	0.112
L86	93998416	8625142	0.082	51160872	65590348	0.282
D87	104176040	8883612	0.147	55742000	64100584	0.150
G88	94040080	8605070	0.085	49562720	61383044	0.238
N89	117720616	8670496	0.263	55389068	59816144	0.080
K90	103189568	8865503	0.141	100584400	80725416	0.197
L91	35023416	822691	0.765	29620446	15817547	0.466
T92	36035868	3124339	0.133	34300976	39211132	0.143
Q93	37242856	1905600	0.488	37094592	30937892	0.166
E94	70416464	2186693	0.689	41776472	32834780	0.214
Q95	50378792	2394817	0.525	40154224	37457740	0.067
K96	34855656	805114	0.769	31116952	20673766	0.336
G97	52757160	663074	0.874	51532752	20294048	0.606
D98	32107684	895124	0.721	32017790	22732204	0.290
K99	41275836	791936	0.808	54966048	22955202	0.582
T101	37201828	853889	0.770	40553928	23593416	0.418
T102	35625700	1197465	0.664	34010648	22831480	0.329
I103	43388664	4589105	0.011	32553186	46857676	0.439
V104	69372168	6400458	0.077	37219076	44913548	0.207
R105	33822964	5437836	0.608	32311688	39383844	0.219
E106	80123480	6929281	0.135	40432288	50036664	0.238
F107	57228940	5699551	0.004	38271188	47130516	0.231
T108	88054464	8131306	0.077	40781024	62275220	0.527
D109	56697220	4780132	0.157	28568392	37258604	0.304
N110	96074048	8283920	0.138	52676776	58198136	0.105
E111	89593432	7141374	0.203	54715776	69202832	0.265
L112	30031082	925762	0.692	31693778	23929902	0.245
T114	15939851	395350	0.752	29302396	12650336	0.568
T115	42106652	1215790	0.711	42548540	24772392	0.418
L116	31003932	823370	0.734	29535744	29692078	0.005
T117	30536578	1186350	0.611	36614776	23963504	0.346
I118	63635652	5815133	0.086	35726864	39794324	0.114
G119	49945288	4162145	0.167	42161864	46365216	0.100
N120	81040824	7139675	0.119	46838724	53944472	0.152
V121	112576056	9949398	0.116	55603628	75957352	0.366
K122	91884104	8060704	0.123	41176568	61103848	0.484
C123	39359176	3922857	0.003	30511132	44030192	0.443
V124	67938072	6449454	0.051	40573196	53708428	0.324
V126	42441488	3743733	0.118	35075312	43388184	0.237
Y127	44466216	3999029	0.101	26752718	30630126	0.145
A129	29458280	3352848	0.138	32795734	45520688	0.388
V130	34709404	3012004	0.132	38839656	38506668	0.009

Supplementary Table S14. Intensity changes during lipid ND titration